Title
Asymmetrically Positioned Flagellar Control Units Regulate Human Sperm Rotation.

Journal
Cell reports, 24(10)

ISSN
2211-1247

Authors
Miller, Melissa R
Kenny, Samuel J
Mannowetz, Nadja
et al.

Publication Date
2018-09-01

DOI
10.1016/j.celrep.2018.08.016

Peer reviewed

Cell Reports

Asymmetrically Positioned Flagellar Control Units Regulate Human Sperm Rotation

Graphical Abstract

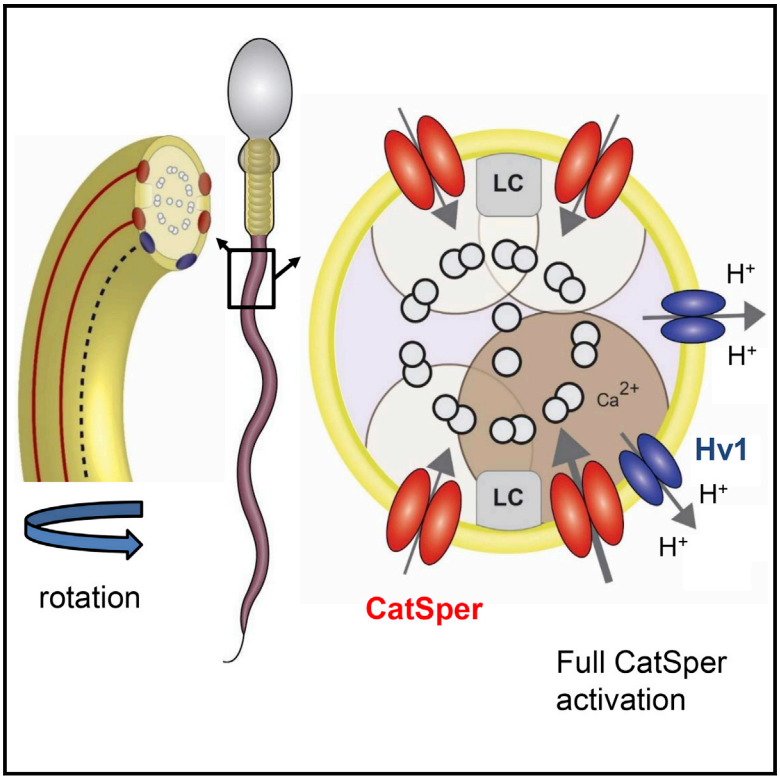

Authors

Melissa R. Miller, Samuel J. Kenny, Nadja Mannowetz, ..., Robert S. Zucker, Ke Xu, Polina V. Lishko

Correspondence

xuk@berkeley.edu (K.X.), lishko@berkeley.edu (P.V.L.)

In Brief

Miller et al. use super-resolution microscopy, electrophysiology, and electron microscopy to show that the sperm proton channel Hv1 forms bilateral lines positioned asymmetrically down the sperm flagellum. Hv1 inhibition leads to a decrease in sperm rotation, suggesting an important role for this channel in sperm motility.

Highlights

- Sperm proton channels form asymmetrically positioned bilateral flagellar lines
- The flagellar ion channels of human sperm are organized in nanodomains
- The nanodomains are comprised of Hv1, CatSper, and ABHD2, ensuring concerted regulation
- Asymmetrical organization of Hv1 is responsible for sperm rotation

Miller et al., 2018, Cell Reports *24*, 2606–2613
September 4, 2018
https://doi.org/10.1016/j.celrep.2018.08.016

CellPress

OPEN ACCESS
CellPress

Cell Reports
Report

Asymmetrically Positioned Flagellar Control Units Regulate Human Sperm Rotation

Melissa R. Miller,[1,4] Samuel J. Kenny,[2,4] Nadja Mannowetz,[1,4] Steven A. Mansell,[1] Michal Wojcik,[2] Sarah Mendoza,[1] Robert S. Zucker,[1] Ke Xu,[2,3,*] and Polina V. Lishko[1,5,*]

[1]Department of Molecular and Cell Biology, University of California, Berkeley, Berkeley, CA 94720, USA
[2]Department of Chemistry, University of California, Berkeley, Berkeley, CA 94720, USA
[3]Chan Zuckerberg Biohub, San Francisco, CA 94158, USA
[4]These authors contributed equally
[5]Lead Contact
*Correspondence: xuk@berkeley.edu (K.X.), lishko@berkeley.edu (P.V.L.)
https://doi.org/10.1016/j.celrep.2018.08.016

SUMMARY

Ion channels control sperm navigation within the female reproductive tract and, thus, are critical for their ability to find and fertilize an egg. The flagellar calcium channel CatSper controls sperm hyperactivated motility and is dependent on an alkaline cytoplasmic pH. The latter is accomplished by either proton transporters or, in human sperm, via the voltage-gated proton channel Hv1. To provide concerted regulation, ion channels and their regulatory proteins must be compartmentalized. Here, we describe flagellar regulatory nanodomains comprised of Hv1, CatSper, and its regulatory protein ABHD2. Super-resolution microscopy revealed that Hv1 is distributed asymmetrically within bilateral longitudinal lines and that inhibition of this channel leads to a decrease in sperm rotation along the long axis. We suggest that specific distribution of flagellar nanodomains provides a structural basis for the selective activation of CatSper and subsequent flagellar rotation. The latter, together with hyperactivated motility, enhances the fertility of sperm.

INTRODUCTION

Fast ciliary responses rely on efficient signal transduction. To achieve rapid signaling, the members of the transduction cascade are tightly compartmentalized into regulatory nanodomains that are located in close proximity (Burns and Pugh, 2010). The organization of the sperm flagellum should follow the same principle because motility cues must propagate rapidly to achieve concerted movement. As mammalian sperm ascend in the oviduct, they have to overcome upstream fluid flow. To succeed in such a task, spermatozoa engage in rheotaxis (Kantsler et al., 2014; Miki and Clapham, 2013) and display specific flagellar motility patterns: hyperactivation and rotation of the flagellum around its longitudinal axis (Ishijima et al., 1992). Such rotation is thought to be linked to calcium (Ca^{2+}) influx and is required for rheotaxis (Miki and Clapham, 2013). Flagellar movement is generated by microtubule sliding powered by ATP hydrolysis (Lindemann and Gibbons, 1975), a pH-dependent process that can also be augmented by an elevation of intraflagellar Ca^{2+} (Brokaw, 1979; Ho et al., 2002; Ishijima et al., 2006; Lindemann et al., 1987; Suarez et al., 1993). Therefore, sperm intracellular Ca^{2+}, pH, and ATP are the key regulatory elements of motility changes; the former two parameters are controlled by ion channels and transporters (Lishko et al., 2012; Ren and Xia, 2010). Distinct nanoscale spatial organization of H^+ and Ca^{2+} channels, therefore, may be a requirement for efficient sperm motion. The principal Ca^{2+} channel of sperm, CatSper (Carlson et al., 2003; Kirichok et al., 2006; Ren et al., 2001), is regulated by intracellular alkalization (Kirichok et al., 2006; Lishko et al., 2012), which, in turn, is under the control of yet-to-be-identified H^+ exchangers and, likely, the voltage-gated proton channel Hv1 (Lishko et al., 2010). The latter mechanism has only been reported for human sperm and is not detected in murine sperm (Lishko et al., 2010). Interestingly, although both human and mouse sperm hyperactivate, only human spermatozoa display full 360° rotation along the long axis, whereas mouse sperm alternate between 180° turns (Babcock et al., 2014). CatSper, which is organized in quadrilateral longitudinal nanodomains along the sperm flagellum (Chung et al., 2014, 2017) is also regulated by species-specific cues (Miller et al., 2015). In human sperm, CatSper is activated by both flagellar alkalinity and progesterone (Lishko et al., 2011; Strünker et al., 2011), whereas, in murine sperm, CatSper is only regulated by the former modality (Kirichok et al., 2006). One candidate for H^+ extrusion in human sperm is Hv1, which moves H^+ unidirectionally toward the extracellular space and raises the intracellular pH (Ramsey et al., 2006; Sasaki et al., 2006). Hv1 is expressed in human sperm (Berger et al., 2017; Lishko et al., 2010), where it can trigger intracellular alkalization, ensuring a favorable condition for activation of the pH-sensitive CatSper (Kirichok et al., 2006). The resulting Ca^{2+} influx directly affects axonemal function and triggers hyperactivation and, perhaps, rotation. Although both motility patterns are required for sperm to detach from the oviductal epithelia (Babcock et al., 2014; Carlson et al., 2005; Ho et al., 2002; Miki and Clapham, 2013), their precise regulatory mechanisms have not been identified. Here we investigated whether the spatio-functional regulation of sperm Hv1, CatSper, and its regulatory protein

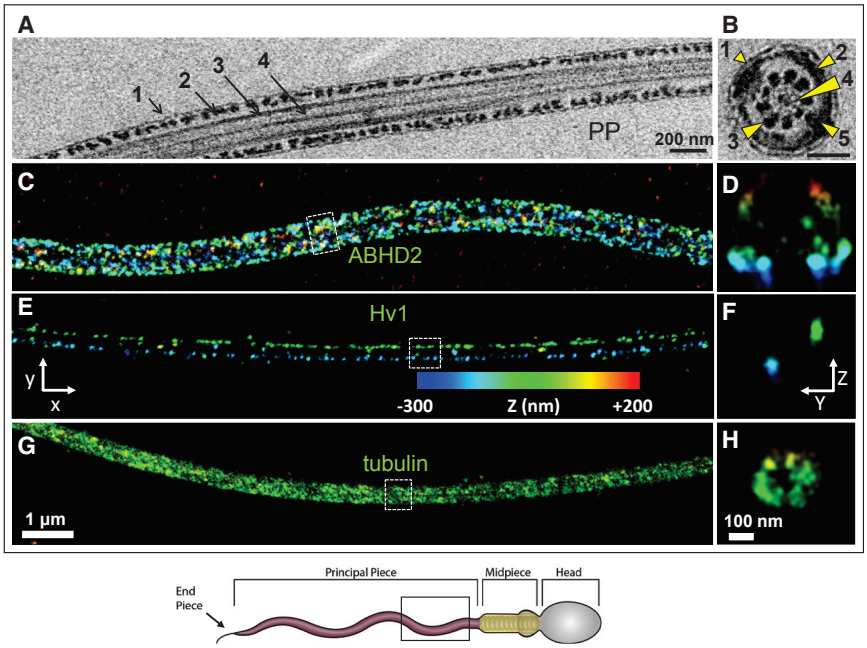

Figure 1. STORM Reveals Distinct Localization of Regulatory Elements within Human Sperm

Bottom: schematic representation of a sperm cell with cellular compartments labeled.

(A–G) *x/y* projections of the sperm flagellum (A, C, E, and G) and cross-sections in *y/z* projections from the corresponding cells (D, F, and H), except for (B), whose cross-section is from a different cell.

(A) TEM of a human sperm principal piece (PP) with structural elements: 1, plasma membrane; 2, fibrous sheath; 3, outer dense fibers; 4, microtubules.

(B) Cross-section of the flagellum at the level of the PP. Elements are as in (A) as well as the following: 5, symmetrically positioned longitudinal columns.

(C and D) Immunostaining for the CatSper regulatory protein ABHD2 (C). The corresponding cross section (D) of the boxed region reveals a quadrilateral arrangement of ABHD2.

(E and F) Immunostaining for Hv1 (E) and the cross-section (F) of the boxed region reveal that Hv1 forms bilateral lines.

(G and H) Immunostaining for β-tubulin (G) and the cross-section (H) of the boxed region used as a marker of the axoneme.

Scale bars, 200 nm (A) and (B), 1 μm (C, E, and G), and 100 nm (D, F, and H). The color in all projections reflects the relative distance from the focal plane along the *z* axis, as shown on the color scale bar in (E). (C)–(H) are 3D-STORM images.

ABHD2 (Miller et al., 2016) could explain these specific motility patterns.

RESULTS

Hv1 Forms Bilateral Lines that Run the Entire Length of the Principal Piece

The sperm principal piece (PP) is a distinct flagellar compartment comprising the majority of the flagellar length that contains the fibrous sheath, a submembrane scaffold structure to which membrane proteins are docked (Eddy et al., 2003; Inaba, 2011; Figures 1A and 1B). Several sperm ion channels and their regulatory elements have been specifically found in the PP region (Lishko et al., 2012). Because sperm flagellar diameters are on sub-micron scales, traditional epi-fluorescence microscopy is not suitable for revealing the details of the distribution of the flagellar proteins because of the method's diffraction-limited resolution of ~250 nm. To overcome this, three-dimensional stochastic optical reconstruction microscopy (3D-STORM) (Huang et al., 2008; Rust et al., 2006) was used to reveal the detailed organization of flagellar elements in human sperm. The same method has been successfully used before to reveal the quadrilateral line arrangement of CatSper (Chung et al., 2014, 2017). In human sperm, CatSper activation has two prerequisites: intraflagellar alkalinity and sperm exposure to progesterone. CatSper activation by progesterone occurs on a timescale of 100 ms (Lishko et al., 2011; Strünker et al., 2011) and is based on the elimination of the CatSper inhibitor 2-arachidonoylglycerol (2-AG) (Miller et al., 2016) by the enzyme ABHD2, which hydrolyzes 2-AG in a progesterone-dependent manner. To enable the rapid progesterone-triggered activation of CatSper, it follows that the turnover of 2-AG should occur in close proximity to the channel itself. Therefore, we hypothesized that, like CatSper in human and mouse sperm (Chung et al., 2017; Chung et al., 2014), its regulator ABHD2 follows a quadrilateral distribution. With 3D-STORM imaging, we assessed the localization of ABHD2 in the flagella of human sperm and found that this enzyme also follows CatSper distribution (Figures 1C and 1D).

According to our previously published immunostaining of human sperm (Lishko et al., 2010), another sperm ion channel, Hv1, is localized to the sperm PP, and this channel is functionally active in epididymal, ejaculated, and capacitated human sperm (Figure S1; Lishko et al., 2010). Therefore, we explored whether Hv1 also follows the quadrilateral pattern of CatSper and ABHD2. Remarkably, 3D-STORM images showed that Hv1 forms the bilateral, and not the quadrilateral, lines along the PP (Figures 1E and 1F; Figure S2), and such localization was preserved upon sperm *in vitro* capacitation (Figure S3A). It has been reported that, during sperm final maturation (also known as capacitation), Hv1 channels undergo N-terminal cleavage (Berger et al., 2017); however, its distinct bilateral distribution pattern upon capacitation does not change (Figures S3B and S3C). Such bilateral distribution of Hv1 clearly differs from the quadrilateral arrangement of the murine and human CatSper (Figure S3D; Chung et al., 2014, 2017). Detailed analysis of the distance between Hv1 lines gave an average distance of 228 ± 19 nm midway down the length of the tail, with 230 ± 15 nm and 250 ± 12 nm for the endpiece region and for the proximal part of the PP, respectively (n = 6 for each measurement;

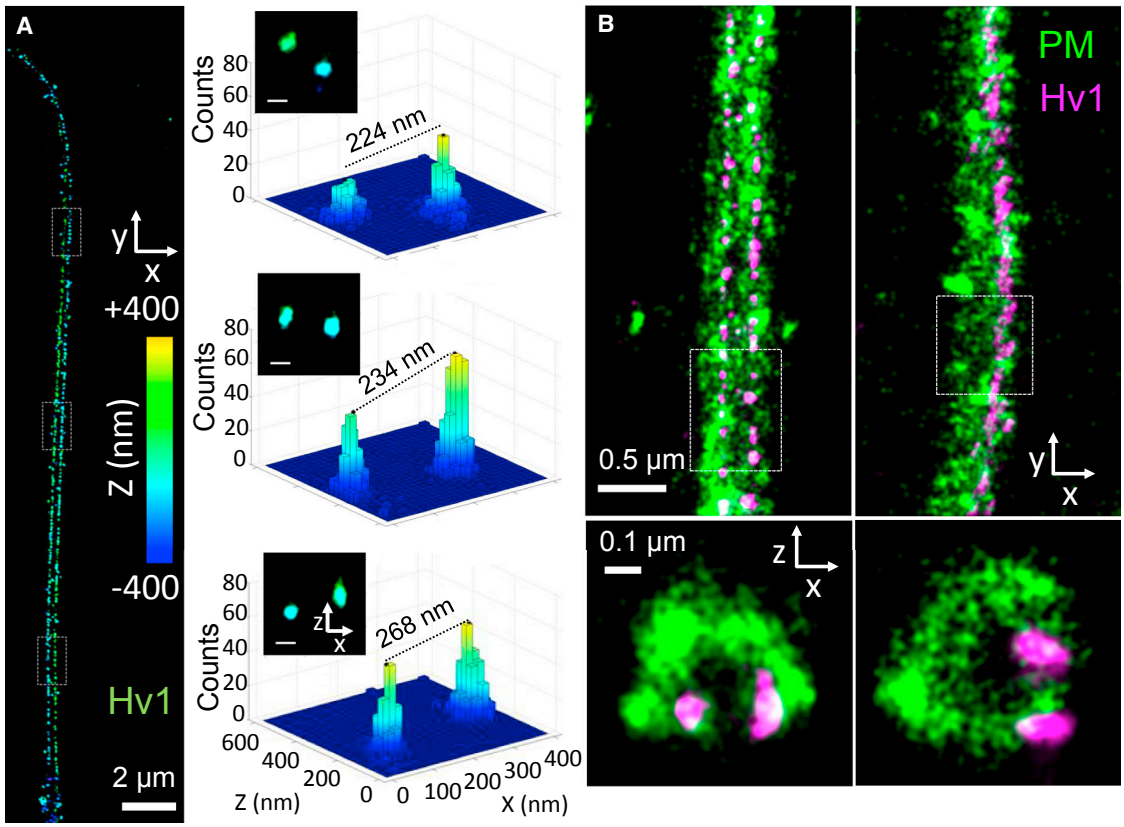

Figure 2. Human Sperm Hv1 Channels Are Organized into Bilateral Domains

(A) Left: 3D-STORM image of Hv1 in a representative sperm flagellum. Right: three regions of interest (ROIs) from *x/y* projections (dotted boxes on the left) were examined, with *x/z* projections shown. For each ROI, the distance between two Hv1 signals was measured as the peak to peak distance from 2D histograms of STORM localizations. Scale bars for the insets represent 100 nm each.

(B) Two-color 3D-STORM image of Hv1 (magenta) and the plasma membrane (green, stained with CM-DiI) in *x/y* and *x/z* projections. The *x/z* projections correspond to the boxes in the *x/y* projections. Shown are two representative flagella.

Figure 2A). This distance is somewhat comparable with the sperm axonemal diameter, as shown by β-tubulin staining (Figures 1G and 1H). However, Hv1 is a membrane protein that must be positioned on the sperm surface, and the flagellar diameter of human sperm is at least double the distance measured between the discrete Hv1 lines. To better understand this discrepancy, we sought to precisely measure the distribution of Hv1 with respect to the flagellar diameter.

The diameter of the human sperm tail varies from 400 to 880 nm, according to the literature (Chemes and Rawe, 2003; Chemes et al., 1998; Serres et al., 1983). This wide range of reported values is likely due to the differences in sample preparation methods, such as sample dehydration, required for electron microscopy, which often distorts the original sample size. A precise measurement of the tail diameter using the same imaging routine and pool of human donors used in this study was essential for the interpretation of the specific Hv1 distribution. Therefore, three different approaches to estimate the diameter at the level of PP were used: bright-field, fluorescence, and electron microscopy methods. Scanning electron microscopy and differential interference contrast (DIC) images (Figures S4A–S4D) indicated an average sperm tail diameter of 570 ± 13 nm (n = 3) and 555 ± 10 nm (n = 7), respectively. To corroborate this measurement, the membrane protein ABHD2 (Miller et al., 2016) was immunolabeled for STORM imaging. Distance measurements taken from STORM images of ABHD2 at the level of the PP of human sperm tails returned similar values of 452 ± 37 nm, 431 ± 13 nm, and 404 ± 27 nm (corresponding to cross-sections of the proximal, middle, and distal positions, as mentioned above for Hv1 (n = 5) (Figures 1C and 1D; Figure S4E). Given that the sperm flagellar diameter is at least 400 nm, and Hv1 is an integral plasma membrane protein with a distance between its lines of ~230 nm, such observations suggest that Hv1 channels are sequestered to one side of the flagellar midline.

Hv1 Is Organized in Asymmetrically Positioned Bilateral Longitudinal Lines

To test this, we performed 2-color 3D-STORM imaging of both human Hv1 and the plasma membrane (PM) using chloromethyl-DiI (CM-DiI), a fixable variant of the lipophilic membrane dye DiI ($DiIC_{18}$) (Shim et al., 2012), to fluorescently label the sperm PM (Figure 2B). Although inhomogeneous staining was noted for certain parts, a phenomenon also observed in other cell types (Pan et al., 2018; Shim et al., 2012), the overall

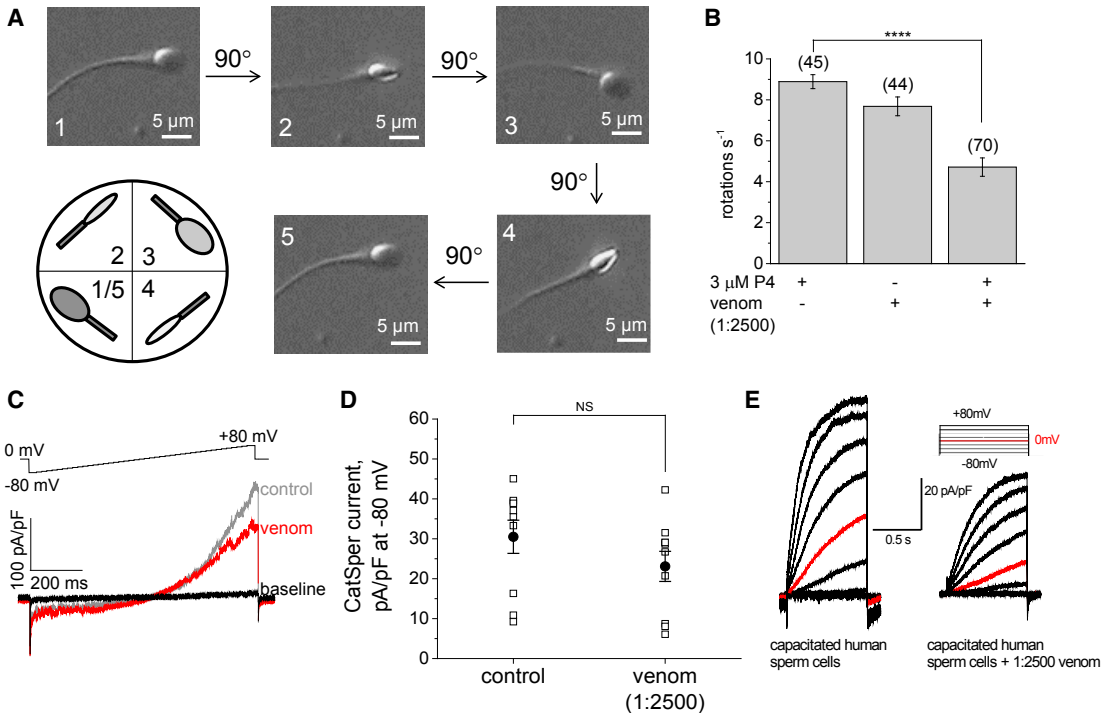

Figure 3. Sperm Rotation Significantly Decreases When CatSper Is Active but Hv1 Is Suppressed

(A) Shown are representative snapshots of a human capacitated sperm performing rotational motion as it turns by 90° within a 15-ms time frame. The diagram below shows the position of the sperm head, which is either parallel to the recording plane (1 or 5 and 3) or perpendicular (2 and 4) to it.

(B) The number of sperm rotations per second produced by human capacitated sperm under control conditions and when subjected to the indicated treatment; ****$p < 0.0001$ (calculated via t test). The experiment was repeated three times with cells from two different human donors.

(C) Venom does not affect human CatSper currents ($I_{CatSper}$). Shown are representative $I_{CatSper}$ in the absence (control, gray) and presence (venom, red) of the venom (same 1:2,500 dilution).

(D) Combined data recorded from 9 individual cells from three different human donors; NS, non-significant. Data are presented as the mean ± SEM, and (n) indicates the number of individual cells analyzed. We were not able to achieve complete inhibition of rotational movement because of the fact that the 1:2,500 venom dilution only inhibits Hv1 by 50% (Lishko et al., 2010; E).

(E) Representative Hv1 current recordings from a control human capacitated sperm cell and the cell capacitated in the presence of tarantula venom. Traces were recorded in response to voltage steps, as indicated, with increasing voltage steps (20 mV increment). The traces recorded at 0 mV are shown in red.

structure of the PM is still well represented, as evidenced by the hollow cross-section. Consistent with single-color experiments, the bilateral lines of Hv1 were positioned asymmetrically to one side of the PM, and this asymmetric distribution was maintained along the whole length of the sperm flagellum (Figures S2 and S5A). Figure S2 demonstrates a situation where the sperm flagellum is fixed with varying degrees of rotation along its long axis. Such images provide a valuable observation that allows the tracing of bilateral lines along the whole length of the flagellum and confirms that the two-line feature is well-maintained through the length of the PP (Figures S2 and S5A). This highly organized and tightly controlled distribution of Hv1 hints at a critical role for the channel in flagellar function.

Hv1 Inhibition Decreases Sperm Rotation along the Long Axis

To reveal the physiological role Hv1 plays in sperm motility, human sperm were capacitated in the presence of an Hv1 inhibitor, a hanatoxin-containing venom from *Grammastola rosea*. As reported previously, such treatment diminishes Hv1 currents in human sperm by 50% ((Lishko et al., 2010; Figure 3E). Hanatoxin is a known inhibitor of voltage-gated channels (Alabi et al., 2007), and the only channel with such characteristics functionally characterized in human sperm is Hv1 (Lishko et al., 2010). As expected, treatment with venom did not alter the inward currents via CatSper (Figures 3C and 3D), and no significant changes in sperm hyperactivation were observed. Next, sperm motility was recorded in the presence of progesterone and/or venom and compared with the motility displayed by untreated sperm. Full 360° rotation (Figures 3A and 3B) was significantly decreased when sperm cells were treated with a combination of venom and progesterone (Figures 3A and 3B; Videos S1, S2, and S3). Interestingly, venom-treated sperm cells not only rotated less but often displayed "partial" 180° rotation by flipping their heads from left to right (Video S3), similar to the motion produced by murine sperm (Babcock et al., 2014; Miki and Clapham, 2013), which lack Hv1 expression ((Lishko et al., 2010; Figure S7). We cannot exclude the possibility that the crude venom used in these studies might have had an unknown effect

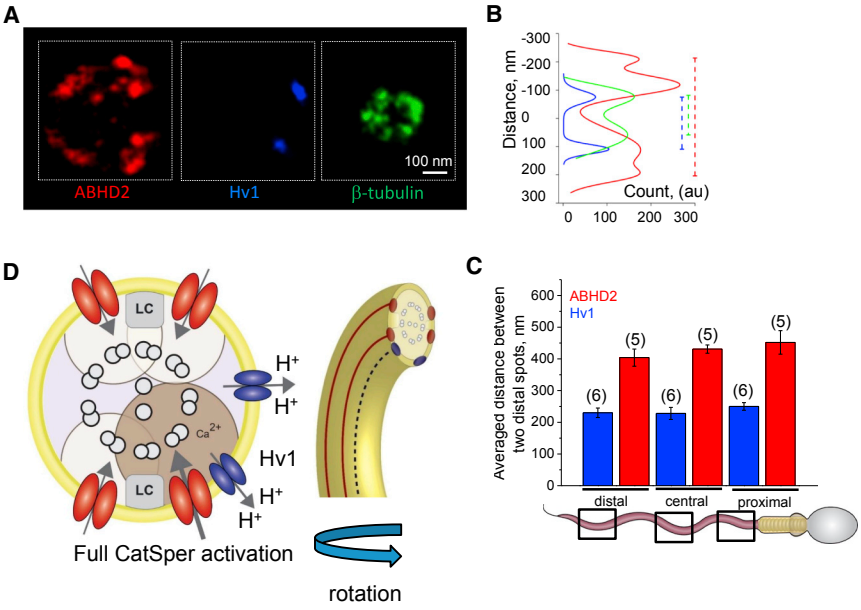

Figure 4. Proposed Nanodomain Structure of the Flagellar Control Units in Human Sperm

(A) Figures 1D, 1F, and 1H in *z*/*y* projections were rotated to align longitudinal columns as described in the Supplemental Experimental Procedures.

(B) Distribution of fluorescence along the *y* axis of Figures 1D, 1F, and 1H to determine distances between the most distal fluorescent peaks.

(C) Averaged distances between fluorescent peaks at three regions along the sperm flagellum for Hv1 and ABHD2; (n) corresponds to the number of cross-sections examined. Data are means ± SEM.

(D) A model suggesting specific localization of CatSper and ABHD2 with respect to Hv1. The model is based on quadrilateral CatSper arrangement (red) in relation to asymmetrical Hv1 lines (blue). H^+ extrusion resulting from Hv1 activity will lead to asymmetrical flagellar alkalization and activation of only a subset of CatSper channels that are located in close proximity to Hv1. This could lead to a flagellar rotation.

on certain hypothetical H^+ exchangers via the venom's potential enzymatic activity. Future studies with yet-to-be-developed Hv1-specific inhibitors will be needed to address this question.

Immunogold Labeling Detects Hv1 in the Same Compartment, as Shown by STORM Imaging

To further elucidate the localization of Hv1 in the PP of human spermatozoa, immunogold labeling and transmission electron microscopy (TEM) were performed (Figures S5B–S5E). The majority of immunogold particles corresponding to Hv1 were found at the fibrous sheath (FS) in cross-sections and longitudinal sections, whereas significantly fewer particles were found at outer dense fibers (ODFs) or microtubules (MTs) (Figures S5B and S5C). The FS is a unique cytoskeletal structure of the sperm PP that consists of two longitudinal columns (LCs; Figure 1B) connected by semicircular ribs (Eddy et al., 2003; Fawcett, 1981). It surrounds the ODFs (Figure 1B) and the sperm axoneme, a cytoskeletal structure comprised of MT doublets (Figures 1A and 1B) arranged in a classical "9 × 2 + 2" pattern. ODFs are sperm tail-specific cytoskeletal structures that support tail bending (Lindemann, 1996). In general, there are nine ODFs (Figures 1B and 4D) in the sperm tail. However, in the PP, two ODFs are replaced by inward projections of the LCs, which divides this part of the sperm tail into two planes—one with three ODFs (3-plane) and one with four ODFs (4-plane) (Figure S5D). Because of the thin (less than 70 nm thick) sections required for TEM and the sparse gold distribution along the sperm tail, we could not observe two immunogold dots in the same cross-section. Therefore, we analyzed immunogold distribution in the FS of individual cross-sections. Gold particles were predominantly found at the 3-plane of the PP, whereas a minor fraction accumulated at the 4-plane (Figures S5D and S5E). Furthermore, gold particles were found preferentially at two distinct clusters at the 3-plane (positions A and B, with 16 and 6 particles, correspondingly; Figure S5D). The distance between centers of the clusters A and B was 172 ± 5 nm (n = 24), which is close to the distance between the Hv1 lines observed with STORM (Figures 1A and 3D; Figure S5A). It is quite possible that the AB cluster could be positioned either on the left or the right side of the 3-plane; however, further co-localization studies are needed to verify the exact localization of the cluster in relation to the chirality of the plane. These results confirm that Hv1 is distributed asymmetrically in the PP of human sperm, whereas CatSper channels cluster symmetrically on either side of the LC (Chung et al., 2014). It is therefore likely that H^+ efflux via Hv1 produces a unilateral alkalization of the flagellum, resulting in the activation of only a subset of all CatSper channels, triggering specific flagellar motion.

Simulation of H^+ Efflux via Hv1 and Its Effect on the Change of Intraflagellar pH

Unilateral alkalization of the sperm intraflagellar environment has two prerequisites: a significant local pH elevation within the Hv1 channel opening or the "mouth" that is facing the intracellular milieu and little or no effect on the distant CatSper channels. We tested the second requirement *in silico* by estimating the intraflagellar pH change in a sperm tail from the action of all Hv1 channels operating simultaneously, both under the conditions of our experiments and under normal physiological conditions. The current corresponding to Figure S1A, right, in human sperm at +80 mV was fit to an exponential rising with a time constant of 0.51 s (Lishko et al., 2010) to a level of 28.2 pA, lasting 3 s and assumed to flow uniformly across the surface of a cylinder, providing a boundary condition to the diffusion equation for hydronium ions solved in cylindrical coordinates and reacting with a native fixed buffer as well as mobile 2-(*N*-morpholino)ethanesulfonic acid (MES) buffer, whose net effect is to slow radial diffusion substantially compared with hydronium ions in pure water. This represents a human sperm tail in the PP region.

Figure S6A shows that this would elevate the submembrane intracellular pH substantially from 6.0 to 7.8, whereas the average pH and the pH at the axonemal core (core pH) would rise to 7.3. Under these conditions, the core and average pH rise sufficiently to significantly activate the rows of CatSper channels (Lishko et al., 2011) opposite of and orthogonal to the row of Hv1 channels. However, such a stimulus is exceptional in both strength and duration; it requires the Hv1 channel to stay open for at least 3 s and does not reflect physiological conditions. Therefore, it was important to estimate what is likely to occur under physiological conditions between successive flagellar flicks with a sperm beat cycle of 24 Hz and rotation of 9 Hz (Figure 3B), assuming a starting pH of 6.0 and a temperature of 37°C. Figure S6B shows the pH now rising only to 6.006 in the time between flagellar flicks, clearly insufficient to influence distant CatSper channels. Note that the simulations overestimate pH rise by ignoring restorative processes such as hydrogen pumps, organelle actions, and metabolic processes.

Next, we estimated the steady-state level of pH that might be reached in the neighborhood of a single hypothetical Hv1 dimer in the presence of natural buffers. It has been reported that Hv1 is organized in dimers *in vivo* (Tombola et al., 2008). Therefore, H^+ are likely to be depleted within 4 nm of the Hv1 mouth so that the pH rises to more than 6.5 within 2.3 nm from the channel mouth (Figure S6C). 2.05 nm from it, the pH rises to 7.2, but only to 6.3 at 2.6 nm away. Under presumed natural conditions at 37°C with more rapid hydronium diffusion and a native mobile buffer replacing MES, the local pH changes are similar. However, local viscosity and tortuosity would raise the local pH even higher. These increases are extremely localized, and a CatSper target within about 2–2.5 nm of the "sink" would be strongly activated by an Hv1 dimer (Figure S6D).

DISCUSSION

Asymmetrical Organization of Hv1 Is Responsible for Sperm Rotation

On their route toward the egg, sperm cells use a mostly symmetrical, snake-like tail motion. However, to overcome the high viscosity of the fallopian tubes or to detach from the tubal ciliated epithelium (Ho et al., 2009), spermatozoa must enhance their flagellar beat. This is achieved by hyperactivation, an asymmetrical flagellar bending that is triggered by Ca^{2+} influx via the CatSper channel (Carlson et al., 2003; Ho et al., 2009), and rotation (Ishijima et al., 1992; Kantsler et al., 2014; Miki and Clapham, 2013). Both motility types are required for rheotaxis, which allows sperm to overcome upstream fluid flow (Ishijima et al., 1992; Kantsler et al., 2014; Miki and Clapham, 2013).

Although CatSper and its regulatory protein ABHD2 are organized in symmetrically positioned quadrilateral lines, the Hv1 channel is distributed differently. Detailed evaluation of the single-color STORM images of ABHD2 (Figures 1C and 1D), Hv1 (Figures 1E and 1F), and β-tubulin, which marks the sperm axoneme (Figures 1G and 1H), and their alignment along LCs, as shown in the Figure 4A, allows visual approximation of their relative distributions (Figures 4A and 1B). Although ABHD2 could be used as a marker for sperm flagellar diameter and has an average distance between lines of at least 400 nm (Figure 4C), the distance between Hv1 bilateral lines is around 230 nm (Figures 2 and 4C). Based on Hv1 immunogold labeling, which indicates a close proximity of one of the Hv1 lines to the LC (Figures S5D and S5E), previously reported evidence that two CatSper lines closely "sandwich" each LC (Chung et al., 2017; Chung et al., 2014), and our assumption that CatSper and ABHD2 are positioned closely to each other, we suggest that one of the Hv1 lines is also in close proximity, if not in the complex, with CatSper channels. This suggestion supports our simulations, which imply a strong interaction of Hv1-induced pH rise on some CatSpers. Taken together, the above observations suggest that the Hv1 channels are sequestered to a single side of the flagellar midline and that one of these lines is positioned in close proximity to a densely packed line of CatSper (Figure 4D).

The asymmetrically positioned H^+-expelling Hv1 could enhance rotation by producing local alkalization when positioned in close proximity to a subset of CatSpers (Figure 4D). Hv1, therefore, has the capacity to fully activate only a subset of CatSper channels, resulting in asymmetrical local Ca^{2+} influx in the tail and, ultimately, creating an asymmetry in axonemal rigidity via calcium-dependent inhibition of the dynein-powered MT sliding. Indeed, by using STORM imaging, we found that Hv1 distribution in the human flagellum follows this prediction (Figures 2 and 4). Although CatSper rows that are positioned opposite of and orthogonal to the row of Hv1 channels still likely produce Ca^{2+} influx, their net Ca^{2+} influx should be smaller compared with that produced by CatSper in close proximity to Hv1 rows (Figure 4D).

The human sperm flagellum has the largest Hv1 current density of all cell types (Lishko et al., 2010). In fact, the Hv1 current is the only H^+ current across the sperm PM that is detectable by the patch-clamp technique. The concentration of a significant number of H^+ channels in such a small cellular domain as a flagellum in close proximity to the pH-sensitive CatSper likely affects sperm physiology in a profound way. Although direct measurement of the intracellular pH changes because of sperm Hv1 activity has not been possible, the fact that Hv1 has a powerful ability to deplete protons in its vicinity has been recently shown (De-la-Rosa et al., 2016). We have confirmed this finding by *in silico* estimation of the steady-state level of pH that might be reached in the neighborhood of a single Hv1 dimer. In fact, the pH rises to 7.2 at 2.05 nm from the Hv1 mouth but only to 6.3 at 2.6 nm away. With these extremely localized pH increases, a CatSper channel complex or its putative pH-sensitive cytoplasmic region (Navarro et al., 2008) must be positioned very close to the Hv1 mouth to be strongly activated by an Hv1. These results support our finding and explain why Hv1 needs to be positioned close to CatSper to ensure local alkalinity, just enough to upregulate only a portion of CatSper channels. Given the fact that Hv1 can significantly change the pH locally (De-la-Rosa et al., 2016), is expressed in human sperm at high density, and is physiologically active (Lishko et al., 2010), Hv1 can produce a significant local alkaline shift. However, such pH changes will occur in nanodomains that are localized only on one side of the flagellum and are likely active only while the sperm cell moves. Because human spermatozoa are fast movers (beat frequency of 24 Hz), it

will require a powerful high-speed recording technique with sufficient sensitivity and spatial resolution to detect fluorescence changes in nanodomains. Such a limitation explains why Hv1-driven intracellular pH changes have not been yet detected in whole flagellar pH imaging.

In conclusion, our results indicate that Hv1 localization in human sperm differs from that of ABHD2 and CatSper and is represented by off-centered bilateral longitudinal lines. This distribution may provide an explanation for sperm rotation along the long axis during sperm rheotaxis. Off-centered positioned Hv1 may selectively and unilaterally alkalinize only a sub-portion of the axoneme, which would, in turn, activate a subset of CatSper channel clusters (Figure 4D). Such asymmetric activation of sperm control units would result in a Ca^{2+} increase in the portion of the flagellum, arrest dynein movement unilaterally, and provide asymmetrical rigidity to the axoneme. This event can fuel a flagellar rotation as the means to relieve the tension. Interestingly, sperm rotation is not dependent on the presence of the head, as observed by rotation displayed by decapitated human sperm flagella (Video S4). Our results indicate that flagellar control units comprised of ABHD2, CatSper, and Hv1 are specifically positioned to ensure fast signal transduction, ultimately orchestrating the complex cellular motion known as hyperactivation and rotation.

EXPERIMENTAL PROCEDURES

Animals

Male C57BL/6 mice were purchased from Harlan Laboratories (Livermore, CA) and kept in the animal facility of the University of California, Berkeley. All experiments were performed in accordance with the NIH Guidelines for Animal Research and approved by the University of California (UC) Berkeley Animal Care and Use Committee under the approved protocol MAUP #R352-012. Animals were humanely euthanized according to Animal Care and Use Committee (ACUC) guidelines, and sperm cells were collected as described previously (Wennemuth et al., 2003).

Healthy Donors and Isolation of Human Ejaculated Spermatozoa

A total of 18 healthy volunteers aged 21–38 were recruited for this study, and all experimental procedures utilizing human-derived samples were approved by the Committee on Human Research at the University of California, Berkeley (protocol number 2013-06-5395). Freshly ejaculated semen samples were obtained by masturbation, and sperm cells were purified by the swim-up technique as described previously (Lishko et al., 2011).

Electrophysiology

All recordings were performed as described previously (Lishko et al., 2011, 2013). Briefly, gigaohm seals between the patch pipette and human sperm were formed at the cytoplasmic droplet. If the cytoplasmic droplet was inconspicuous, then spermatozoa were patched at the neck region. See Supplemental Experimental Procedures for details.

STORM Imaging

3D-STORM (Huang et al., 2008; Rust et al., 2006) was carried out on a home-built setup, as reported previously(Wojcik et al., 2015). Typical localization accuracies (SDs), as determined by repeatedly localizing the same single clusters in the samples in this study, were ~12 nm in plane (*xy*) and ~20 nm in depth (*z*), corresponding to full width at half maximum (FWHM) values of 28 and 47 nm, respectively. These results are in good agreement with the typical resolution of 3D-STORM (Huang et al., 2008). See Supplemental Experimental Procedures for details.

Additional procedures could be found in the Supplemental Experimental Procedures.

SUPPLEMENTAL INFORMATION

Supplemental Information includes Supplemental Experimental Procedures, seven figures, and four videos and can be found with this article online at https://doi.org/10.1016/j.celrep.2018.08.016.

ACKNOWLEDGMENTS

This work was supported by R01GM111802 and R21HD081403 from NIH, the Alfred P. Sloan Award, the Packer Wentz Endowment Will (to P.V.L.), the Pew Biomedical Scholars Award (to P.V.L. and K.X.), the Rose Hill Innovator Award (to P.V.L.), and the NSF under CHE-1554717 (to K.X.). K.X. is a Chan Zuckerberg Biohub investigator. We thank Dr. Jean-Ju Chung for sharing the anti-CatSper delta antibody and Drs. Reena Zalpuri and Kent McDonald from the UC Berkeley EM facility for help with TEM. We also thank Dr. James F. Smith (UCSF) for sharing samples of human epididymal fluid, obtained with patient consent. Publication made possible in part by support from the Berkeley Research Impact Initiative (BRII) sponsored by the UC Berkeley Library.

AUTHOR CONTRIBUTIONS

M.R.M. and P.V.L. conceived the project and designed the experiments. M.R.M., S.J.K., K.X., and P.V.L. wrote the manuscript. M.R.M. performed immunostaining and electrophysiology. P.V.L. performed pilot electrophysiology experiments. S.J.K., M.W., and K.X. performed STORM and SEM sample preparation, image acquisition, and data analysis. S.A.M. helped with pilot electrophysiology experiments from animal sperm cells. N.M. performed immunoelectron staining, CatSper electrophysiology, and sperm motility analysis. S.M. helped with sperm motility acquisition and analysis. R.S.Z. performed *in silico* measurements and analyses and commented on the manuscript. P.V.L. and K.X. supervised and led the project. All authors discussed the results and commented on the manuscript.

DECLARATION OF INTERESTS

The authors declare no competing interests.

Received: March 7, 2018
Revised: June 26, 2018
Accepted: August 6, 2018
Published: September 4, 2018; Corrected online: March 5, 2019

REFERENCES

Alabi, A.A., Bahamonde, M.I., Jung, H.J., Kim, J.I., and Swartz, K.J. (2007). Portability of paddle motif function and pharmacology in voltage sensors. Nature *450*, 370–375.

Babcock, D.F., Wandernoth, P.M., and Wennemuth, G. (2014). Episodic rolling and transient attachments create diversity in sperm swimming behavior. BMC Biol. *12*, 67.

Berger, T.K., Fußhöller, D.M., Goodwin, N., Bönigk, W., Müller, A., Dokani Khesroshahi, N., Brenker, C., Wachten, D., Krause, E., Kaupp, U.B., and Strünker, T. (2017). Post-translational cleavage of Hv1 in human sperm tunes pH- and voltage-dependent gating. J. Physiol. *595*, 1533–1546.

Brokaw, C.J. (1979). Calcium-induced asymmetrical beating of triton-demembranated sea urchin sperm flagella. J. Cell Biol. *82*, 401–411.

Burns, M.E., and Pugh, E.N., Jr. (2010). Lessons from photoreceptors: turning off g-protein signaling in living cells. Physiology (Bethesda) *25*, 72–84.

Carlson, A.E., Westenbroek, R.E., Quill, T., Ren, D., Clapham, D.E., Hille, B., Garbers, D.L., and Babcock, D.F. (2003). CatSper1 required for evoked Ca2+ entry and control of flagellar function in sperm. Proc. Natl. Acad. Sci. USA *100*, 14864–14868.

Carlson, A.E., Quill, T.A., Westenbroek, R.E., Schuh, S.M., Hille, B., and Babcock, D.F. (2005). Identical phenotypes of CatSper1 and CatSper2 null sperm. J. Biol. Chem. *280*, 32238–32244.

Chemes, E.H., and Rawe, Y.V. (2003). Sperm pathology: a step beyond descriptive morphology. Origin, characterization and fertility potential of abnormal sperm phenotypes in infertile men. Hum. Reprod. Update *9*, 405–428.

Chemes, H.E., Olmedo, S.B., Carrere, C., Oses, R., Carizza, C., Leisner, M., and Blaquier, J. (1998). Ultrastructural pathology of the sperm flagellum: association between flagellar pathology and fertility prognosis in severely asthenozoospermic men. Hum. Reprod. *13*, 2521–2526.

Chung, J.J., Shim, S.H., Everley, R.A., Gygi, S.P., Zhuang, X., and Clapham, D.E. (2014). Structurally distinct $Ca^{(2+)}$ signaling domains of sperm flagella orchestrate tyrosine phosphorylation and motility. Cell *157*, 808–822.

Chung, J.J., Miki, K., Kim, D., Shim, S.H., Shi, H.F., Hwang, J.Y., Cai, X., Iseri, Y., Zhuang, X., and Clapham, D.E. (2017). CatSperζ regulates the structural continuity of sperm Ca2+ signaling domains and is required for normal fertility. eLife *6*, e23082.

De-la-Rosa, V., Suárez-Delgado, E., Rangel-Yescas, G.E., and Islas, L.D. (2016). Currents through Hv1 channels deplete protons in their vicinity. J. Gen. Physiol. *147*, 127–136.

Eddy, E.M., Toshimori, K., and O'Brien, D.A. (2003). Fibrous sheath of mammalian spermatozoa. Microsc. Res. Tech. *61*, 103–115.

Fawcett, D.W. (1981). Sperm Flagellum. In The Cell (W.B. Saunders, Co.), pp. 604–624.

Ho, H.C., Granish, K.A., and Suarez, S.S. (2002). Hyperactivated motility of bull sperm is triggered at the axoneme by Ca2+ and not cAMP. Dev. Biol. *250*, 208–217.

Ho, K., Wolff, C.A., and Suarez, S.S. (2009). CatSper-null mutant spermatozoa are unable to ascend beyond the oviductal reservoir. Reprod. Fertil. Dev. *21*, 345–350.

Huang, B., Wang, W., Bates, M., and Zhuang, X. (2008). Three-dimensional super-resolution imaging by stochastic optical reconstruction microscopy. Science *319*, 810–813.

Inaba, K. (2011). Sperm flagella: comparative and phylogenetic perspectives of protein components. Mol. Hum. Reprod. *17*, 524–538.

Ishijima, S., Hamaguchi, M.S., Naruse, M., Ishijima, S.A., and Hamaguchi, Y. (1992). Rotational movement of a spermatozoon around its long axis. J. Exp. Biol. *163*, 15–31.

Ishijima, S., Mohri, H., Overstreet, J.W., and Yudin, A.I. (2006). Hyperactivation of monkey spermatozoa is triggered by Ca2+ and completed by cAMP. Mol. Reprod. Dev. *73*, 1129–1139.

Kantsler, V., Dunkel, J., Blayney, M., and Goldstein, R.E. (2014). Rheotaxis facilitates upstream navigation of mammalian sperm cells. eLife *3*, e02403.

Kirichok, Y., Navarro, B., and Clapham, D.E. (2006). Whole-cell patch-clamp measurements of spermatozoa reveal an alkaline-activated Ca2+ channel. Nature *439*, 737–740.

Lindemann, C.B. (1996). Functional significance of the outer dense fibers of mammalian sperm examined by computer simulations with the geometric clutch model. Cell Motil. Cytoskeleton *34*, 258–270.

Lindemann, C.B., and Gibbons, I.R. (1975). Adenosine triphosphate-induced motility and sliding of filaments in mammalian sperm extracted with Triton X-100. J. Cell Biol. *65*, 147–162.

Lindemann, C.B., Goltz, J.S., and Kanous, K.S. (1987). Regulation of activation state and flagellar wave form in epididymal rat sperm: evidence for the involvement of both Ca^{2+} and cAMP. Cell Motil. Cytoskeleton *8*, 324–332.

Lishko, P.V., Botchkina, I.L., Fedorenko, A., and Kirichok, Y. (2010). Acid extrusion from human spermatozoa is mediated by flagellar voltage-gated proton channel. Cell *140*, 327–337.

Lishko, P.V., Botchkina, I.L., and Kirichok, Y. (2011). Progesterone activates the principal Ca^{2+} channel of human sperm. Nature *471*, 387–391.

Lishko, P.V., Kirichok, Y., Ren, D., Navarro, B., Chung, J.J., and Clapham, D.E. (2012). The control of male fertility by spermatozoan ion channels. Annu. Rev. Physiol. *74*, 453–475.

Lishko, P., Clapham, D.E., Navarro, B., and Kirichok, Y. (2013). Sperm patch-clamp. Methods Enzymol. *525*, 59–83.

Miki, K., and Clapham, D.E. (2013). Rheotaxis guides mammalian sperm. Curr. Biol. *23*, 443–452.

Miller, M.R., Mansell, S.A., Meyers, S.A., and Lishko, P.V. (2015). Flagellar ion channels of sperm: similarities and differences between species. Cell Calcium *58*, 105–113.

Miller, M.R., Mannowetz, N., Iavarone, A.T., Safavi, R., Gracheva, E.O., Smith, J.F., Hill, R.Z., Bautista, D.M., Kirichok, Y., and Lishko, P.V. (2016). Unconventional endocannabinoid signaling governs sperm activation via the sex hormone progesterone. Science *352*, 555–559.

Navarro, B., Kirichok, Y., Chung, J.J., and Clapham, D.E. (2008). Ion channels that control fertility in mammalian spermatozoa. Int. J. Dev. Biol. *52*, 607–613.

Pan, L., Yan, R., Li, W., and Xu, K. (2018). Super-Resolution Microscopy Reveals the Native Ultrastructure of the Erythrocyte Cytoskeleton. Cell Rep. *22*, 1151–1158.

Ramsey, I.S., Moran, M.M., Chong, J.A., and Clapham, D.E. (2006). A voltage-gated proton-selective channel lacking the pore domain. Nature *440*, 1213–1216.

Ren, D., and Xia, J. (2010). Calcium signaling through CatSper channels in mammalian fertilization. Physiology (Bethesda) *25*, 165–175.

Ren, D., Navarro, B., Perez, G., Jackson, A.C., Hsu, S., Shi, Q., Tilly, J.L., and Clapham, D.E. (2001). A sperm ion channel required for sperm motility and male fertility. Nature *413*, 603–609.

Rust, M.J., Bates, M., and Zhuang, X. (2006). Sub-diffraction-limit imaging by stochastic optical reconstruction microscopy (STORM). Nat. Methods *3*, 793–795.

Sasaki, M., Takagi, M., and Okamura, Y. (2006). A voltage sensor-domain protein is a voltage-gated proton channel. Science *312*, 589–592.

Serres, C., Escalier, D., and David, G. (1983). Ultrastructural morphometry of the human sperm flagellum with a stereological analysis of the lengths of the dense fibres. Biol. Cell *49*, 153–161.

Shim, S.H., Xia, C., Zhong, G., Babcock, H.P., Vaughan, J.C., Huang, B., Wang, X., Xu, C., Bi, G.Q., and Zhuang, X. (2012). Super-resolution fluorescence imaging of organelles in live cells with photoswitchable membrane probes. Proc. Natl. Acad. Sci. USA *109*, 13978–13983.

Strünker, T., Goodwin, N., Brenker, C., Kashikar, N.D., Weyand, I., Seifert, R., and Kaupp, U.B. (2011). The CatSper channel mediates progesterone-induced Ca^{2+} influx in human sperm. Nature *471*, 382–386.

Suarez, S.S., Varosi, S.M., and Dai, X. (1993). Intracellular calcium increases with hyperactivation in intact, moving hamster sperm and oscillates with the flagellar beat cycle. Proc. Natl. Acad. Sci. USA *90*, 4660–4664.

Tombola, F., Ulbrich, M.H., and Isacoff, E.Y. (2008). The voltage-gated proton channel Hv1 has two pores, each controlled by one voltage sensor. Neuron *58*, 546–556.

Wennemuth, G., Babcock, D.F., and Hille, B. (2003). Calcium clearance mechanisms of mouse sperm. J. Gen. Physiol. *122*, 115–128.

Wojcik, M., Hauser, M., Li, W., Moon, S., and Xu, K. (2015). Graphene-enabled electron microscopy and correlated super-resolution microscopy of wet cells. Nat. Commun. *6*, 7384.

Cell Reports, Volume *24*

Supplemental Information

Asymmetrically Positioned Flagellar Control Units Regulate Human Sperm Rotation

Melissa R. Miller, Samuel J. Kenny, Nadja Mannowetz, Steven A. Mansell, Michal Wojcik, Sarah Mendoza, Robert S. Zucker, Ke Xu, and Polina V. Lishko

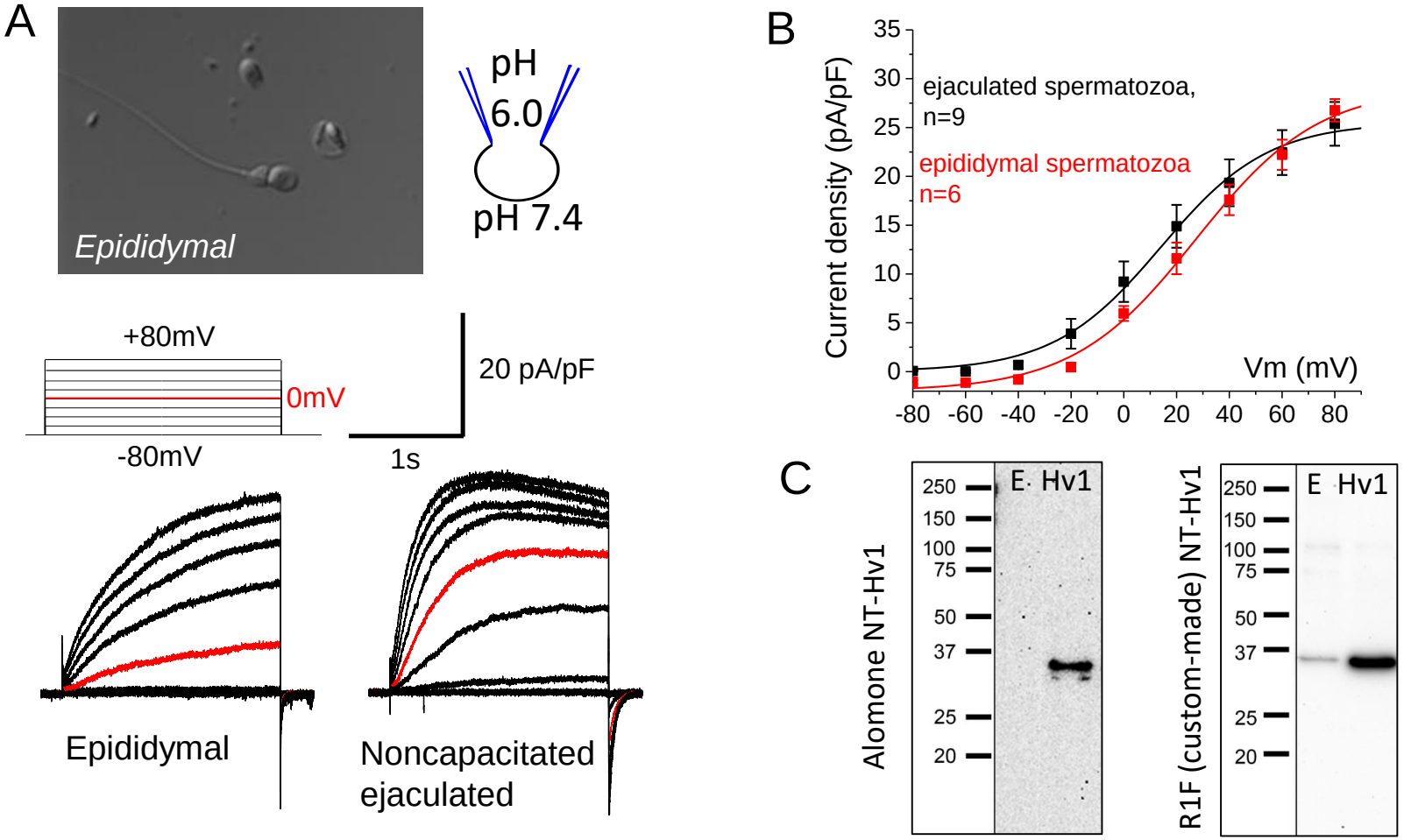

Figure S1. Hv1 is present in human epidydimal and ejaculated sperm. Related to Figures 1, 2 and 3. (A) Representative recordings from a human noncapacitated ejaculated spermatozoon and a sperm cell isolated from human *cauda epididymis*. Traces were recorded in response to voltage steps from the holding potential of -80mV with increasing voltage steps (20 mV increment) up to +80 mV. The traces recorded at 0 mV are shown in red. The insert shows a picture of human epididymal sperm cells. The diagram depicts a recording pipette with the cell attached and indicates intracellular pH and pH in the bath. (B) Averaged current density shows human sperm Hv1 current in both sperm preparations. Data are means +/- S.E.M, and n indicates the number of sperm cells tested. (C) Representative western blots showing CHO cell lysates from cells transiently transfected with empty vector (E), or expression vector bearing human Hv1 (Hv1). Both primary antibodies were used in 1:10,000 dilution. The blots were probed with a commercially available antibody from Alomone Labs (Alomone NT-Hv1) and an in-house custom-generated anti-Hv1 antibody (R1F NT-Hv1, reported in (Lishko et al., 2010)).

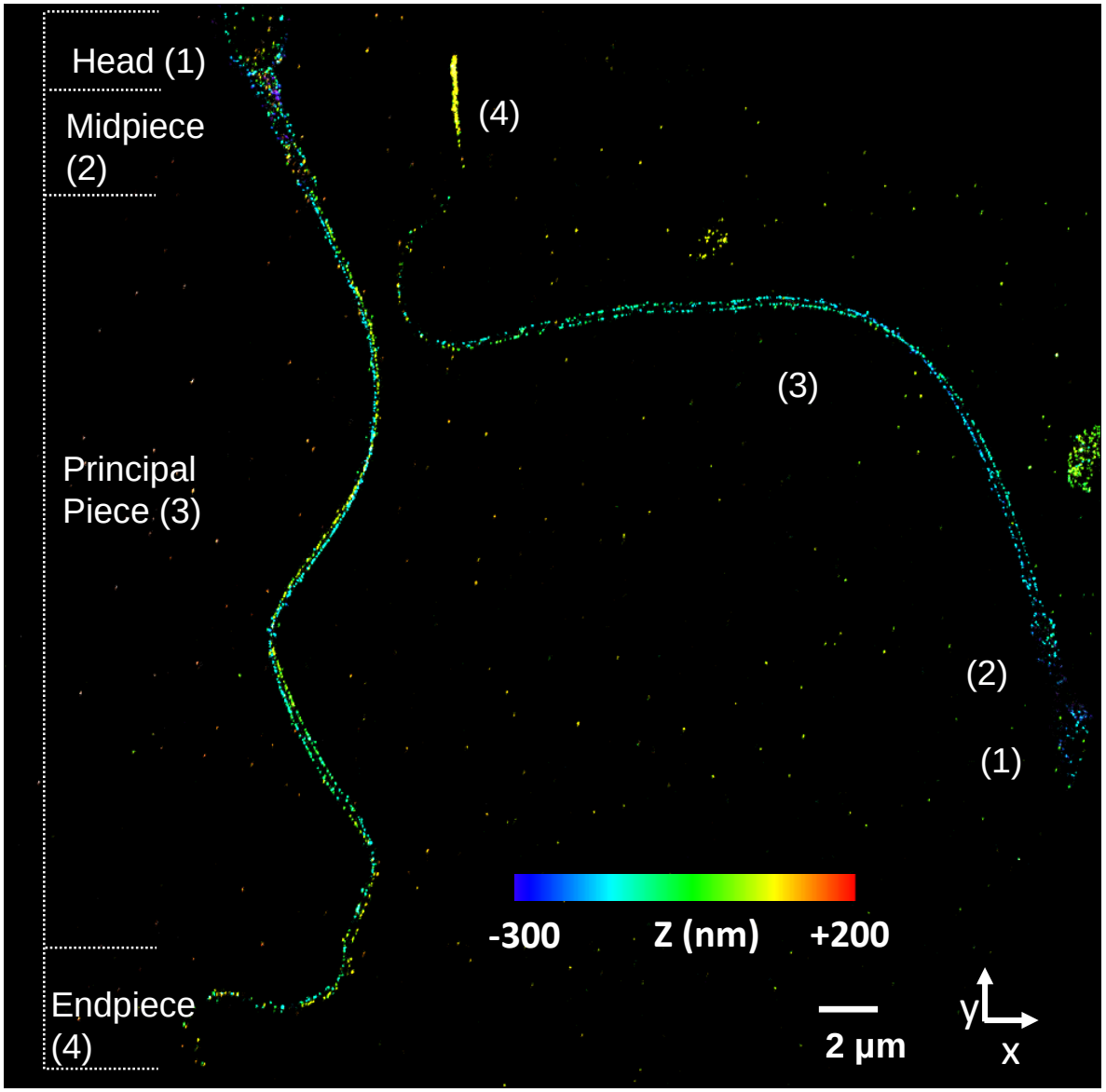

Figure S2. STORM imaging of Hv1 in human sperm cells. Related to Figures 1 and 2. Shown are two human sperm cells immunostained for Hv1. The color reflects the relative distance from the focal plane along the z axis as shown with the color scale bar. Sperm regions (the head, midpiece, principal piece and the endpiece are indicated).

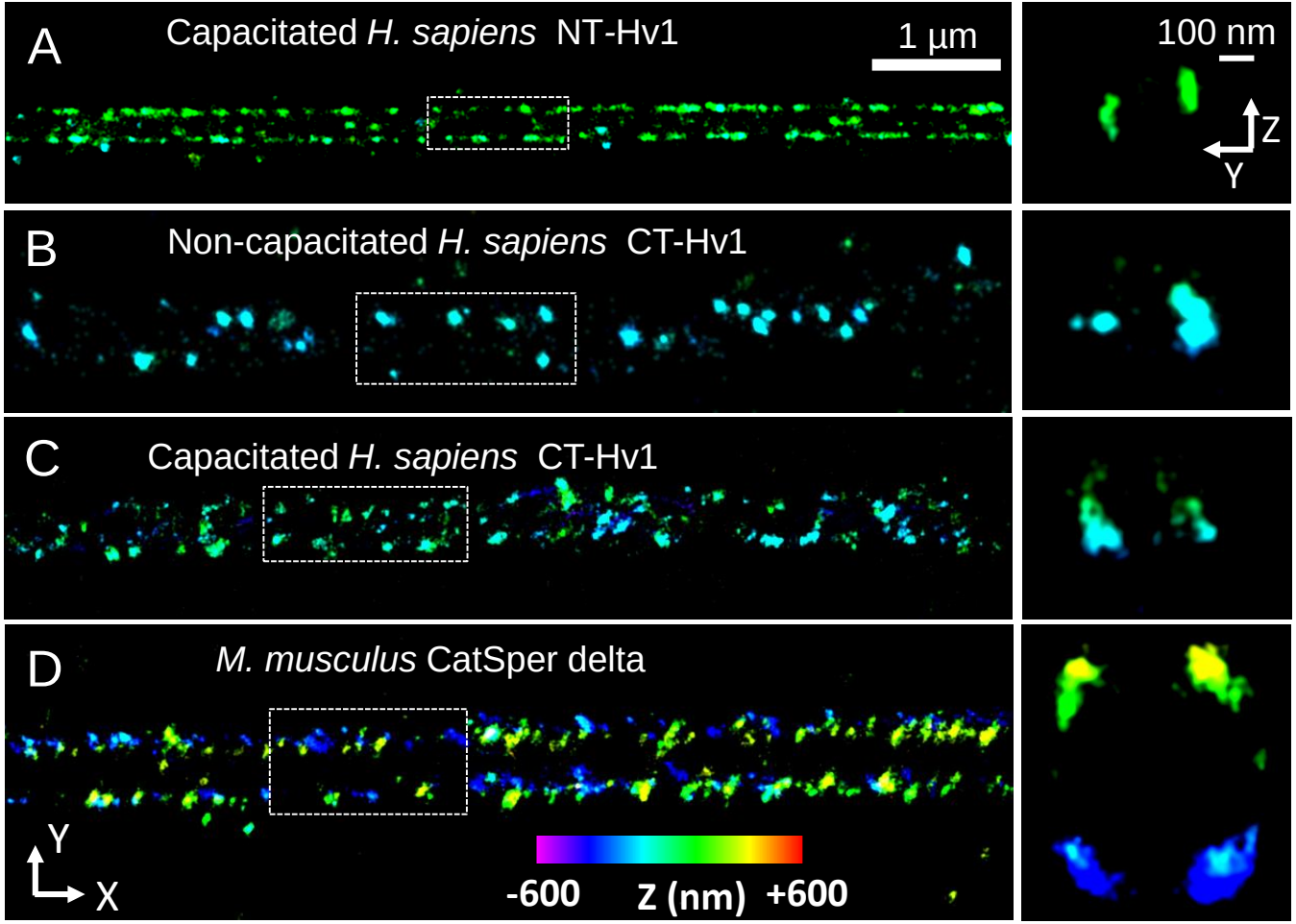

Figure S3. STORM imaging of the human and mouse sperm flagella. 3D-STORM images related to Figures 1 and 2. (A) Left panel: immunostaining of a human capacitated spermatozoon probed with an anti-Hv1 antibody (Alomone, N-terminal antigen). Right panel: the cross section from the same flagellum (from the boxed region) shows double-line Hv1 staining. (B) Left panel: immunostaining of a human noncapacitated spermatozoon probed with an anti-Hv1 antibody (Sigma, C-terminal antigen). Right panel: the cross section from the same flagellum (from the boxed region) shows double-line Hv1 staining. (C) Left panel: immunostaining of a human capacitated spermatozoon probed with an anti-Hv1 antibody (Sigma, C-terminal antigen). Right panel: the cross section from the same flagellum (from the boxed region) shows unchanged double-line Hv1 staining. (D) Left panel: immunostaining of a mouse caudal spermatozoon probed with an anti-CatSper antibody. Right panel: the cross section from the same flagellum (from the boxed region) shows a quadrilateral CatSper arrangement. Left panels in (A-D) show the x/y projections of the sperm flagellum, while right panels show cross-sections in y/z projections from the corresponding cells. Color reflects the relative distance from the focal plane along the z axis as shown on the color scale bar in (D). Scale bars on x/y projections are 1 mm, while scale bars on y/z projections are 100 nm.

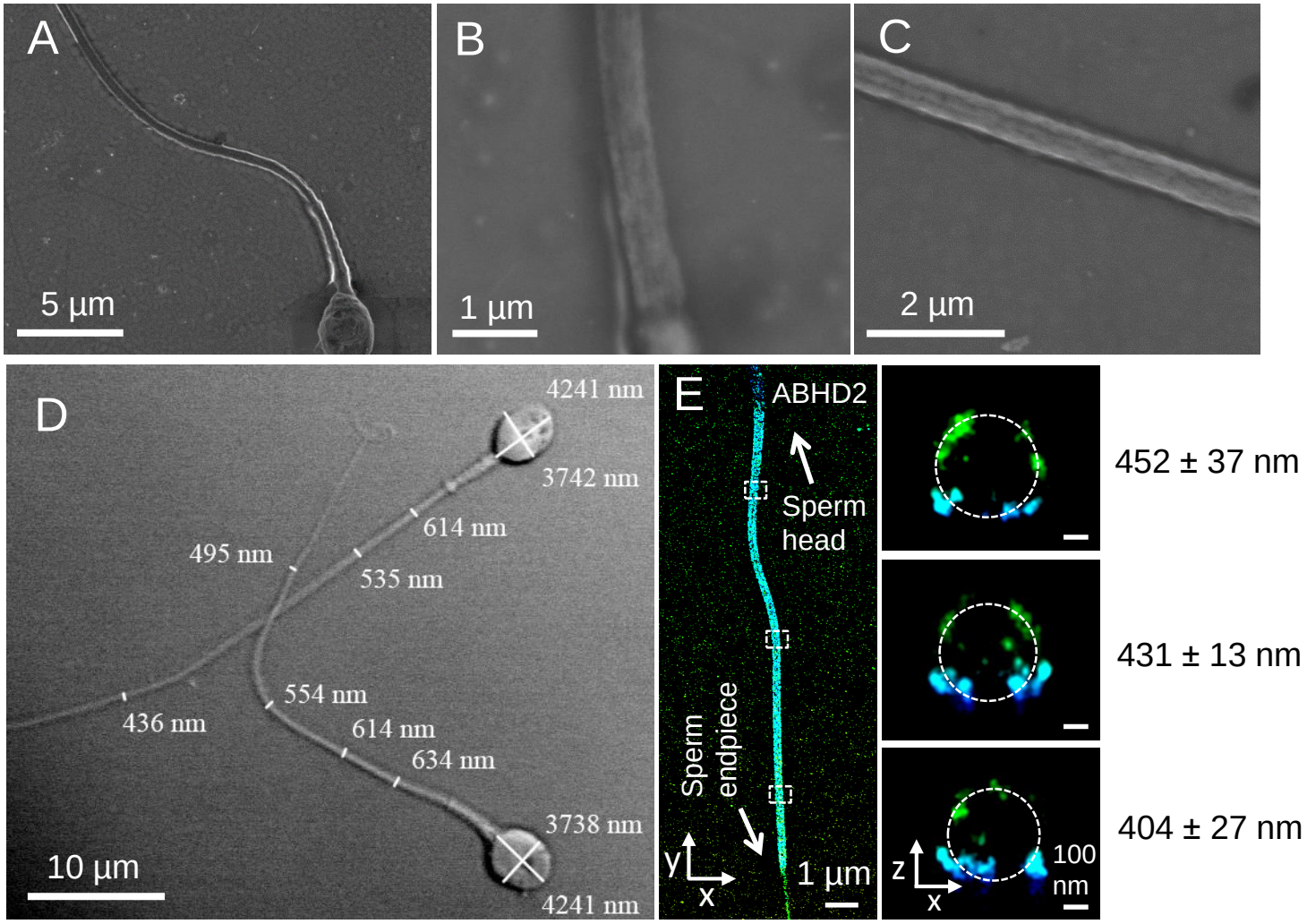

Figure S4. Scanning electron microscopy (SEM), differential interference contrast (DIC) and STORM imaging of ABHD2 to estimate the average flagellar diameter of the human sperm tail. Related to Figures 1 and 4. (A-C) Representative images of several human sperm revealed by SEM of graphene-protected, non-dehydrated samples. (D) Representative DIC image of human spermatozoa. (E) STORM imaging of the human sperm flagellum probed with anti-ABHD2 antibody as shown in Figure 1C. Cross sections (right panels) were taken from corresponding regions of the x/y projection (left panel) as indicated by dotted boxes; from top to bottom, ROIs were selected at distances of 5, 14, and 20 µm from the beginning of the principal piece (PP). Right panels show averaged distances between two distal ABHD2 spots acquired at the corresponding tail segments; data are means +/- S.E.M. with n=5. Scale bars are 1 µm (left); 100 nm (right). 3D color scale is as shown in Fig. 1E.

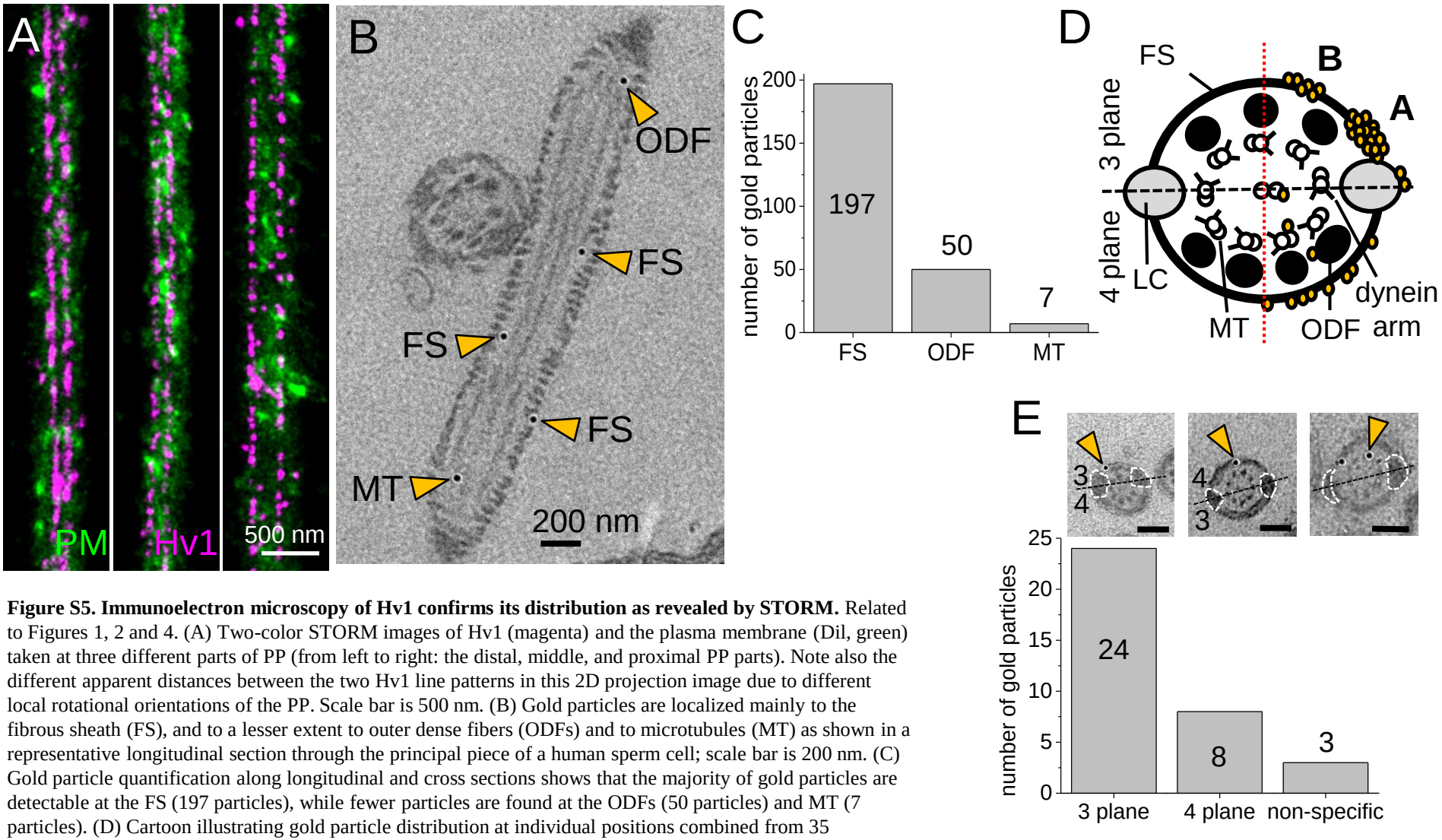

Figure S5. Immunoelectron microscopy of Hv1 confirms its distribution as revealed by STORM. Related to Figures 1, 2 and 4. (A) Two-color STORM images of Hv1 (magenta) and the plasma membrane (DiI, green) taken at three different parts of PP (from left to right: the distal, middle, and proximal PP parts). Note also the different apparent distances between the two Hv1 line patterns in this 2D projection image due to different local rotational orientations of the PP. Scale bar is 500 nm. (B) Gold particles are localized mainly to the fibrous sheath (FS), and to a lesser extent to outer dense fibers (ODFs) and to microtubules (MT) as shown in a representative longitudinal section through the principal piece of a human sperm cell; scale bar is 200 nm. (C) Gold particle quantification along longitudinal and cross sections shows that the majority of gold particles are detectable at the FS (197 particles), while fewer particles are found at the ODFs (50 particles) and MT (7 particles). (D) Cartoon illustrating gold particle distribution at individual positions combined from 35 individual cross-sections. Since it is not possible to determine if gold particles were located on the left or on the right side of the sperm tail, all gold particles were plotted onto the right side. Gold particles are found predominantly on the "3 plane" forming two distinct clusters: cluster "A" (6 particles) and cluster "B" (16 particles). (E) Gold particle quantification of individual cross sections at the FS of the 3 plane (24 particles) and 4 plane (8 particles) as well as at unspecific regions (ODFs or MT; 3 particles); scale bars are 200 nm. For this analysis only PP cross sections with clearly identifiable LCs and ODFs were included.

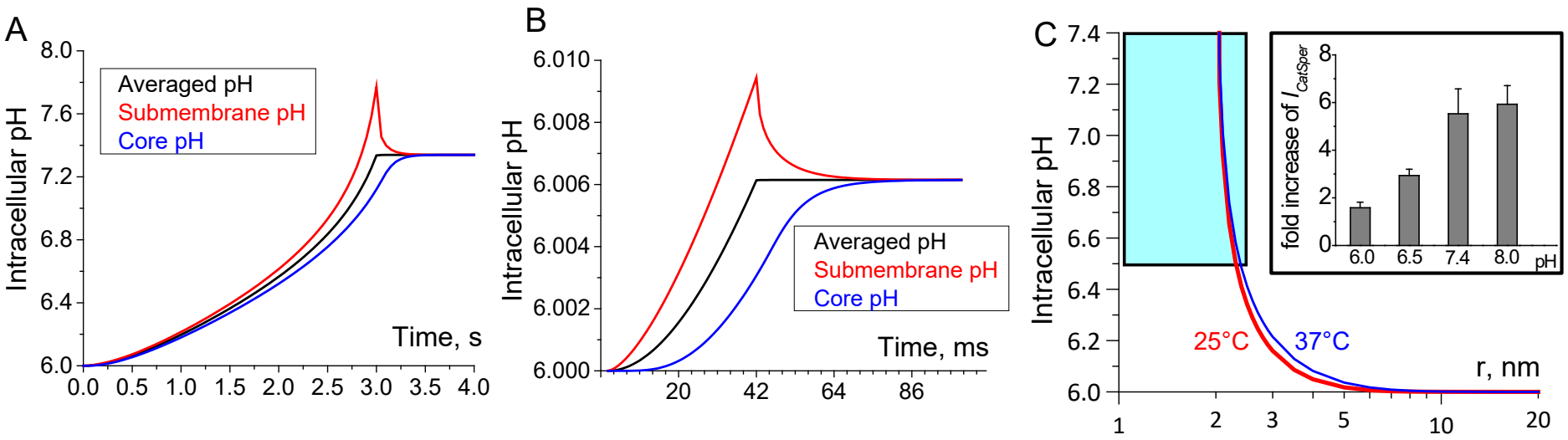

Figure S6. Simulated sperm intraflagellar pH (pHi) changes caused by Hv1 activity. Related to Figure 4. (A) The total pH change in a whole sperm tail principal piece from the action of all Hv1 channels operating simultaneously, modeled by H^+ current passing uniformly across the surface of a cylinder representing a human sperm tail at the principal piece region: 0.5-µm-diameter and 40-µm-long. Sperm tail pH was calculated for three positions: submembrane (red; estimated as ~ 5 nm shell below the plasma membrane), core (at the center of a sperm axoneme, blue), and total volume-averaged (black). Parameters were chosen based on those in Fig. S1A (right panel), with a voltage clamp of +80 mV, while the channel stayed open for 3 s. (B) The effects of H^+ efflux under physiological conditions, with a 0 mV membrane potential and activation time of 40 ms, corresponding to the interval between flagellar flicks. Note that while proton efflux was simulated uniformly for simplicity, efflux along asymmetrical lines of Hv1 channels would probably cause alkalinization and affect distant CatSper channels in a way similar to the "core pH" (blue line). No pH restorative processes are included. (C) H^+ efflux from an Hv1 dimer is represented as a point sink from a semi-infinite space opening at time zero. The local steady-state pH changes near the dimer are plotted for conditions corresponding to the experiments at 25°C (red) and physiological conditions at 37°C (blue). The inset (extracted from data shown in Figure 2d from (Lishko et al., 2011)) plots the fold increase in CatSper inward current activated by 500 nM progesterone in response to CatSper activity in the absence of the progesterone at different intraflagellar pHs. A significant effect begins above pH 6.5, and this region is indicated by a blue square. (D) A separation of up to 2.5 nm between Hv1 and CatSper channels in overlapping rows would fall within this region and allow CatSper to be directly regulated by Hv1. All simulations include a native fixed buffer, plus a native mobile buffer in (B) and (C, blue), which were replaced by 100mM MES in (A) and (C, red).

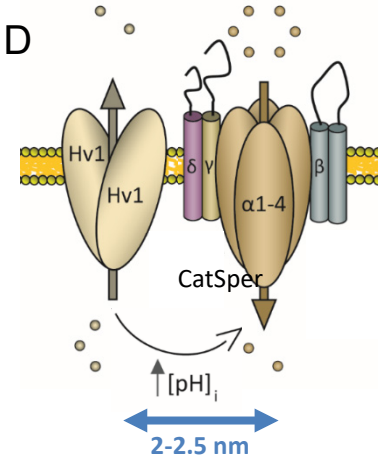

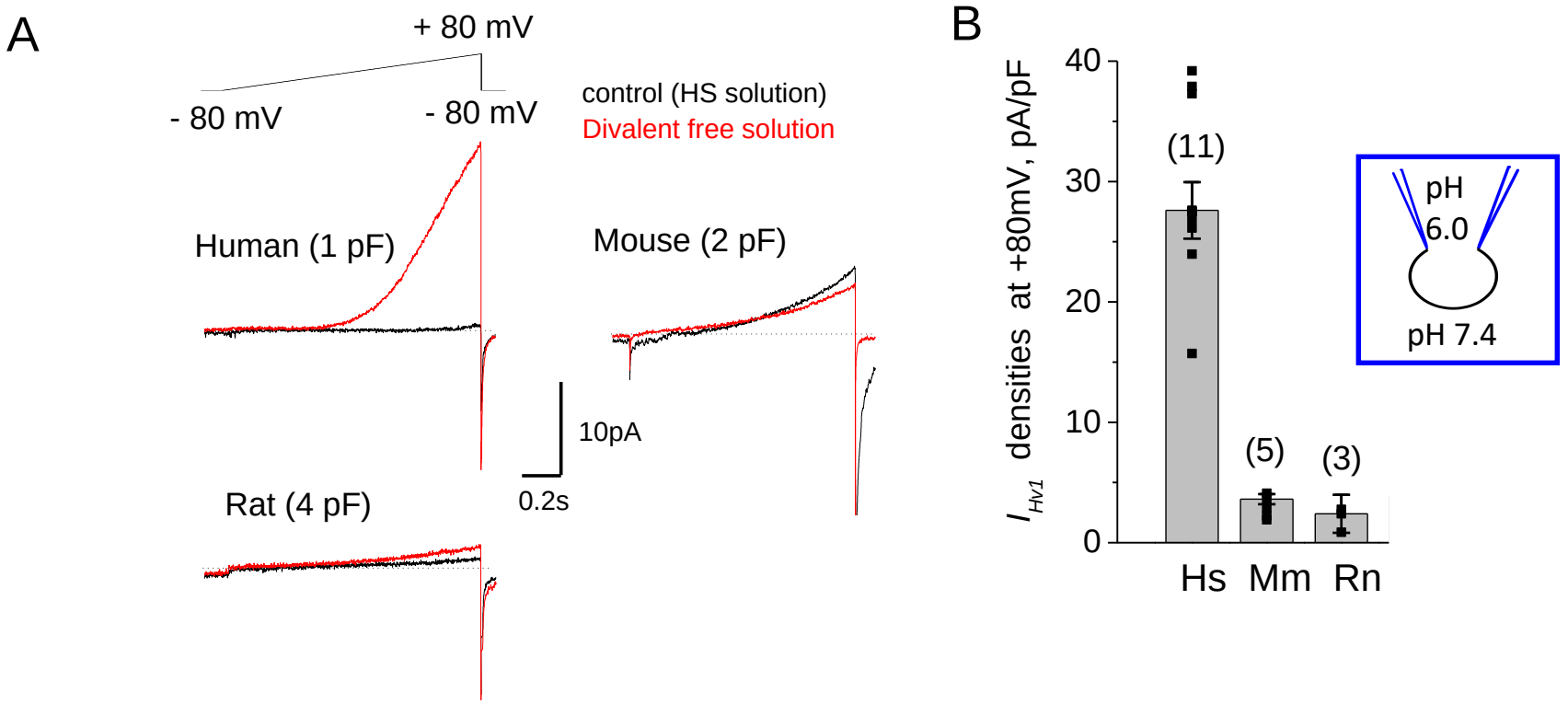

Figure S7. The presence of the functional proton channel Hv1 in mammalian sperm. Related to Figures 1, 2 and 3. (A) Representative Hv1 current recording from sperm cells of different species as indicated. (B) Averaged currents (I_{Hv1}) density recordings from sperm of 3 different species; (n)- indicates the number of experiments. Data are means +/- S.E.M. Abbreviations are: noncapacitated human (Hs; *Homo sapiens*), mouse (Mm; *Mus musculus*), rat (Rn; *Rattus norvegicus*).

Supplemental Experimental Procedures

Reagents. Progesterone was purchased from CalBiochem (EMD Millipore, Darmstadt, Germany). All other compounds were from Sigma-Aldrich (St. Louis, MO) unless otherwise specified. Primary antibodies: rabbit anti-ABHD2 IgG (C14214) was obtained from Assay Biotech (San Francisco, CA), and from One World Lab. Monoclonal mouse anti-beta-tubulin IgG1 (T5201) were purchased from Sigma-Aldrich. The anti-actin antibody (ab3280) was from Abcam (Cambridge, MA). Rabbit anti-Hv1 IgGs (AHC-001; ALA, against N-terminus) were from Alomone Labs (Jerusalem, Israel), rabbit anti-Hv1 IgG (HPA039329; against C-terminus) were from Sigma, and affinity purified rabbit-anti-Hv1 (R1F, against N-terminus) IgG was custom-made purified (Lishko et al., 2010). The CatSper-delta antibody was received from Jean-Ju Chung (Chung et al., 2014). Secondary antibodies: anti-rabbit AF647 or AF488; anti-mouse AF647; anti-mouse AF647 were from Invitrogen. Anti-rabbit CF680 and anti-rat CF680 were made by conjugating CF680 NHS-ester (Biotium) to unlabeled corresponding secondary antibodies (Jackson Immunoresearch). Human (NLH-06) and mouse (NLM-06) testis lysates were purchased from G-Biosciences (Geno Technology). *Grammostola rosea* venom was purchased from Spider Pharm (Yarnell, AZ; https://spiderpharm.com).

Electrophysiology. Seals were formed in high saline (HS) solution containing: 130 mM NaCl, 5 mM KCl, 1 mM $MgSO_4$, 2 mM $CaCl_2$, 5 mM glucose, 1 mM sodium pyruvate, 10 mM lactic acid, 20 mM HEPES, pH 7.4 adjusted with NaOH, 320mOsm/L. Transition into the whole-cell mode was performed by applying light suction in combination with short voltage pulses. Access resistance was 25-40 MΩ. Cells were stimulated every 5 s. Data were sampled at 2-5 kHz and filtered at 1 kHz. For proton currents: pipettes for whole-cell patch-clamp recordings (20–30 MΩ) were filled with 135 mM N-methyl-D-glucamine (NMDG), 5 mM ethylene glycol tetraacetic acid (EGTA), and 100 mM MES and pH adjusted to 6.0 with methanesulfonic acid. Proton currents were recorded in divalent-free (DVF) bath solution comprising 130 mM NMDG, 100 mM HEPES, and 1 mM EDTA and pH adjusted to 7.4 with methanesulfonic acid. For monovalent CatSper recordings- (Figure 3C), pipettes (11-17 MΩ) were filled with (in mM): 130 Cs-methanesulfonate, 70 HEPES, 3 EGTA, 2 EDTA, 0.5 Tris-HCl, pH 7.4 adjusted with CsOH. Bath divalent-free (DVF) solution for recording of monovalent CatSper currents contained (in mM): 140 Cs-methanesulfonate, 40 HEPES, 1 EDTA, pH 7.4 adjusted with CsOH. All electrophysiology experiments were performed at ambient temperature and currents elicited by voltage ramps or step protocols as indicated for each individual experiment Data were analyzed with OriginPro 9.0 and Clampfit 9.2. Statistical data were calculated as the mean ± S.E.M., and (n) indicates number of experiments.

STORM imaging. Dye-labeled cell samples were mounted on glass coverslips with a standard STORM imaging buffer consisting of 5% (w/v) glucose, 100 mM cysteamine, 0.8 mg/mL glucose oxidase, and 40 µg/mL catalase in 1M Tris-HCl (pH 7.5) (Huang et al., 2008; Rust et al., 2006). Coverslips were sealed using Cytoseal 60. STORM imaging was performed on a homebuilt setup based on a modified Nikon Eclipse Ti-E inverted fluorescence microscope using a Nikon CFI Plan Apo λ 100x oil immersion objective (NA 1.45). This setup (Wojcik et al., 2015) is based on well-characterized systems (Huang et al., 2008; Rust et al., 2006), and has been used in many previous publications (Pan et al., 2018; Wojcik et al., 2015; Zhang et al., 2015).

Dye molecules were photoswitched to the dark state and imaged using either 647- or 560-nm lasers (MPB Communications); these lasers were passed through an acousto-optic tunable filter and introduced through a single-mode optical fiber into the back focal plane of the microscope and onto the sample at intensities of ~2 kW cm^{-2}. A uniform Gaussian beam profile was thus achieved with no noticeable speckle effects. A translation stage was used to shift the laser beams towards the edge of the objective so that light reached the sample at incident angles slightly smaller than the critical angle of the glass-water interface, thus illuminating ~1 μm into the sample (near-TIRF mode). A 405-nm laser was used concurrently with either the 647- or 560-nm lasers to reactivate fluorophores into the emitting state. The power of the 405-nm laser (typical range 0-1 W cm^{-2}) was adjusted during image acquisition so that at any given instant, only a small, optically resolvable fraction of the fluorophores in the sample was in the emitting state. Emission was recorded with an Andor iXon Ultra 897 EM-CCD camera with 100× EM-gain at a framerate of 110 Hz, for a total of ~80,000 frames per image. This relatively large frame number ensures that enough localizations are accumulated to produce a faithful presentation of the labeled structure. Each STORM image typically contained 10^5-10^6 single-molecule localizations across the frame size of ~40 μm × 40 μm. Each labeled cluster often contained >10 single-molecule localizations due to the labeling of multiple dye molecules through secondary immunofluorescence (below) and the reversible photoswitching of each dye molecule.

For 3D-STORM imaging, a cylindrical lens of 1 m focal length was inserted into the imaging path so that images of single molecules were elongated in opposite directions for molecules on the proximal and distal sides of the focal plane. Two-color imaging was performed via sequential imaging of targets labeled by Alexa Fluor 647 and CM-DiI. Nanoscale color channel alignment was achieved by adding 0.002% (w/v) yellow-green fluorescent beads into the STORM imaging buffer (FluoSpheres; Thermo F8811). Adherent beads near the cell to be imaged were activated and imaged in each color channel for the entire imaging duration. The resulting localizations were used to align the color channels in 3 dimensions. For the color coding showed in Figures 1E, 2A, S2, and S3, the same color coding was used for the in-plane (XY) and cross-sectional (YZ and XZ) views, and the color bars for the z scales were given in the XY panels. The representative regions of interest that were at appropriate angles we selected, so that the YZ and XZ views give useful cross-sectional views.

To generate image shown in Figure 4A, the transverse sections of panels (D), (F) and (H) from Figure 1 in z/y projections were rotated to align longitudinal columns (LC) in the vertical position as indicated by the vertically positioned gap in beta-tubulin staining. As LCs occupy a larger part of the flagellar interior, they create an imaging artifact, resulting in the diminished signal from axonemal markers around LC area. As reported previously by Chung et al.(Chung et al., 2017; Chung et al., 2014), two CatSper lines “sandwich” each LC, therefore LC position on the transverse CatSper staining could be easily deduced as the center of the shortest line connecting two CatSper spots. Since we assume that CatSper and ABHD2 are in close proximity to each other, we assume that ABHD2 should follow the same pattern distribution as CatSper, and LC positions on the transverse ABHD2 sections could be deduced the same way. However, two possibilities exist in aligning Hv1 signal. According to electron microscopy data (Figure S5), Hv1 lines are positioned on a single side of the axoneme, with one of the lines in close proximity to LC. Therefore, Hv1 lines can be positioned either on the axonemal right side or the left side (Figure 4D). Either position didn’t change the conclusions reached in this work.

Image processing. The raw STORM data were analyzed according to previously described methods (Huang et al., 2008; Rust et al., 2006). Briefly, optical astigmatism elongated images of single-molecules along either the vertical or horizontal axis for molecules above or below the focal plane, respectively. Intensity-based thresholding was used to detect single molecule blinking events, which were subsequently fit to elliptical 2D Gaussians. The resulting centroid positions were used to determine the super-resolved lateral positions of each single molecule. Axial positions were determined by a calibration curve which mapped the ellipticity of each fitted Gaussian to its position above or below the focal plane. The calibration curve was generated by imaging and measuring the ellipticities of fluorescent beads adhered to a coverglass, while moving the sample smoothly through the focal plane (Huang et al., 2008)(Huang *et al.*, 2018).

Geometric characterization of STORM cross sections. Distance measurements were obtained from STORM data using custom MATLAB routines. For a direct width comparison of different targets, 1D histograms were generated on straight, cropped sections of sperm tails for the coordinate perpendicular to the tail axis. Histogram bin position and counts were plotted and fit to a 2-term Gaussian, from which the FWHM was extracted. A precise measure of sperm membrane diameter was obtained by fitting cross-sectional STORM data from ABHD2 to a circle using a least mean squares minimization algorithm (Thomas and Chan, 1989). Hv1 geometry was characterized by binning XZ- or YZ- cross-sectional STORM data into 2D histograms. Peaks from these histograms were used to define the centers of distinct clusters of molecular coordinates; the distance between the centers of mass of these clusters was computed.

Isolation of human epididymal spermatozoa. Men with proven fertility who were undergoing sperm retrieval procedures in the UCSF Center for Reproductive Health agreed to donate unused portions of surgical specimens. As part of the ongoing IRB-approved UCSF LIFE (Lifestyle, Fertility, and Evaluation) study, men enrolled in the study had a documented history of prior paternity and had undergone a vasectomy in the past. As part of routine clinical care, these men elected to undergo a sperm retrieval procedure (microscopic epididymal sperm aspiration) combined with in vitro fertilization (IVF) or a vasectomy reversal. Aliquots of epididymal fluids were used for the present study with patients' consents. Epididymal spermatozoa were isolated from the samples as described(Smith et al., 2013).

In vitro capacitation. The capacitation medium (HSB/BSA) consisted of HS solution supplemented with 15 mM $NaHCO_3$ and 5% BSA. Human sperm cells were capacitated for 4-5 h at 37°C and 5% CO_2 in HSB/BSA alone or in HSB/BSA spiked with either 3 µM P4, G. rosea crude venom (1:2500) or a combination of venom (1:2500) plus P4 (3 µM).

Assessment of sperm rotation. 100 µl of the sperm suspension were transferred to the recording chamber. Free-swimming sperm were examined on an inverted microscope (Olympus IX-71) equipped with a 60 ×/1.20 W objective. 500 ms-long movies were taken with a digital high-speed Memrecam GX-1 camera (NAC Image Technology, Simi Valley, CA) and collected with the Memrecam GXLink software, version 3.20 (NAC Image Technology) at 1,000 frames per second from a 640 × 480 pixel region of the camera chip and stored in AVI format. Movies were replayed with ImageJ version 1.44o (http://rsb.info.nih.gov/ij/) to assess the number of rotations of individual cells. Since each movie was only 500 ms long, values were multiplied by 2 to obtain rotations per second. Data were evaluated with the OriginPro 9.0 software (Origin Lab,

Northampton, MA) and expressed as means ± SEM. Statistical significance (t-test) was indicated by: ****, $p < 0.0001$, ***, $p < 0.001$, **, $p < 0.005$ and *, $p < 0.05$. No variation between human donors were noticed, and control and venom- treated samples were donor matched for the analysis. While control untreated sperm cells can engage in full 360-degree rotation (or rolling) movement, the venom treated cells only rotate half way: producing 180-degree rotation. We have recorded sperm rotation along the longitudinal axis based on the changes in the reflected light intensity and changes in the head position as indicated in the diagram (Figure 3A and Supplementary Movies 1-3). We have analyzed each frame by looking at the "blinking" of the head as an indication of the rotatory movement, as well as by determining the entire head position to discriminate between a complete 360-degree rotation and a partial, 180-degree flipping. We have also determined rotation frequency of the full 360-degree rotating sperm only and ignored non-rotating sperm cells. In addition, we have asked three independent observers to analyze the movies in the unbiased way and all three respondents interpreted the movies correctly, pointing to the venom/P4 -treated cell as those that show decreased rotation.

Immunocytochemistry. Purified spermatozoa (concentration ~10^7 cells/ml) were plated onto coverslips in HS and allowed to attach for 10 min. The cells were fixed with 4% paraformaldehyde (PFA) in 1x PBS (Phosphate Buffered Saline) for 10 min and washed twice with PBS. Additional fixation was performed for samples not subsequently labeled with CM-DiI using 100% ice-cold methanol for 1 min with two washes in 1x PBS. Cells were permeabilized for 5 min with 0.25% Triton or 0.1% saponin in PBS followed by two PBS washes and blocked for one hour in PBS supplemented with 3% gamma-globulin free BSA (bovine serum albumin, fraction V). Immunostaining was performed in blocking solution. Detergent-treated cells were incubated with primary antibodies overnight at 4°C. After extensive washing in PBS, secondary antibodies were added for 60 min. The dilutions of primary antibodies were 1:100 and secondaries were 1:200. For membrane visualization, cells were then incubated with the lipophilic membrane dye CM-DiI (3H-Indolium, 5-[[[4-(chloromethyl)benzoyl]amino]methyl]-2-[3-(1,3-dihydro-3,3-dimethyl-1-octadecyl-2H-indol-2-ylidene)-1-propenyl]-3,3-dimethyl-1-octadecyl-chloride, Invitrogen) at 5 μM in PBS for 20 min at room temperature. After 3 washes with PBS, cells meant for confocal imaging were mounted with ProLong Gold antifade with DAPI reagent (Life Technologies, Carlsbad, CA) or if cells were to be used for super-resolution imaging, coverslips were post-fixed for 10 min in 3.7% PFA and 0.1% glutaraldehyde, washed twice with PBS and stored in PBS until imaging.

Scanning electron microscopy (SEM). SEM was performed on fully hydrated sperm cells via graphene protection, as described previously (Wojcik et al., 2015). Briefly, fixed cells on coverglass were stained with 2% uranyl acetate (SPI 02624) in water for 2 hours and thoroughly rinsed. Monolayer CVD graphene on copper foil was obtained from Graphene Supermarket (Calverton, NY). To cover cells with graphene, the hydrated coverslip containing the cells was used to scoop up a graphene-PMMA stack floating on water. The stack was allowed to adhere to the sample for ~10 min in air. To remove PMMA, the sample was dipped in anisole or acetone for 2 min, and rinsed off briefly in isopropyl alcohol. The graphene-covered coverslip was mounted on a standard metallic sample mount with carbon tape, and a small amount of silver colloid paint (Ted Pella 16031) was used to create a conductive bridge between graphene and the sample mount. SEM imaging was performed under standard secondary electron mode on an FEI Quanta 3D FEG

system at normal operational vacuum (~10^{-5} torr). Calibration of magnification was verified with a replica of a 2,160 lines/mm waffle-pattern diffraction grating (Ted Pella 604-A).

Immunogold-labelling and transmission electron microscopy. After swim-up purification sperm were allowed to sediment. Cells were fixed with PBS/8% PFA for 10 min. After permeabilization with PBS/0.1% saponin for 15 min and blocking with PBS/5% BSA for 45 min, sperm were incubated with a 1:50 dilution of rabbit anti-Hv1 IgG (#AHC001; Alomone Labs, Jerusalem, Israel) in PBS/5% BSA overnight at 4°C. After excessive washing in PBS sperm were incubated for 1 h with goat anti-rabbit antibody conjugated to nanogold (1:40 in PBS/5% BSA; Electron Microscopy Sciences, Hatfield, PA, USA). After three washing steps in PBS, cells were fixed for 15 min with 2.5% glutaraldehyde in PBS. Cells were transferred to agarose and treated for 30 min with 0.5% OsO_4 in 0.1 M cacodylate buffer (pH 7.4). After dehydration in a graded ethanol series and propylene oxide the pellet was embedded in Epon 812 resin. After polymerization for 72 h at 65°C, 70 nm thick sections were cut on a Reichert Ultracut-E microtome (Leica, Wetzlar, Germany) and mounted onto formvar-coated nickel grids (Electron Microscopy Sciences, Hatfield, PA, USA). After signal enhancement with the HQ silver enhancement kit (Nanoprobes, Yaphank, NY, USA) for 8 min the grids were treated with 2% uranyl acetate and lead citrate for 4 min, respectively. Samples were examined on a Tecnai 12 transmission electron microscope (FEI, Hillsboro, OR, USA) equipped with an Ultrascan 1000 camera (Gatan, Pleasanton, CA, USA).

Measurement of the distance between two clusters "A" and "B" in EM cross sections. The straight distance between the center of each LC and corresponding gold particles in the fibrous sheath (FS) of individual cross sections was measured. Positions of gold particles, which clustered in position "A" or "B" at the 3 plane were averaged to calculate the mean distance of positions "A" (mean A) and "B" (mean B) from each LC. To measure the distance between [mean A] and [mean B], we projected the centers of each LCs to [mean A] and [mean B] from three individual cross sections. Next, three triangles were plotted with defining sides as follows. Triangle 1: **a** = distance between [mean A] and ipsilateral LC, **d** = distance between both LCs (aka flagellar diameter), and **a'** = distance between [mean A] and contralateral LC. The angle between **a** and **d** was defined as **A**. Triangle 2: **b** = distance between [mean B] and ipsilateral LC, **b'** = distance between [mean B] and contralateral LC, and **d**. The angle between **b** and **d** was defined as **B.** Triangle 3: **a**, **b** and **c** = distance between [mean A] and [mean B]. The angle between **a** and **b** was defined as **C.** To determine angles **A** and **B**, the law of cosines was used: $(a')^2 = a^2 + d^2 - 2ad\cos(A)$ and $(b')^2 = b^2 + d^2 - 2bd\cos(B)$. Since C= A-B, we have determined **c** as: $c^2 = a^2 + b^2 - 2ab\cos(C)$.

Simulation of proton efflux via Hv1 and its effect on the intraflagellar pH change. For the first *in silico* estimation of the global pH rise in the sperm tail (Fig. S6A) we numerically solved a reaction-diffusion scheme, applying Fick's Second Law of Diffusion along with equilibrium binding reactions of H^+ with fixed and mobile buffers, to calculate the spatio-temporal changes in pH within a sperm tail in response to H^+ efflux at the surface. We implemented a program written in BASIC in which a cylindrical radial diffusion model used a finite-difference-element numerical solution of the diffusion. At each time step, flux between concentric cylindrical shells followed Fick's Law for H^+, diffusing as hydronium ions. Assuming free and bound forms of the diffusible buffer diffused at the same rate, the total concentration of the diffusible buffer remains uniform

and constant. The surface shell included an efflux in the form of an exponential fit to the proton current of Fig. S1A.

Each diffusion step was followed by a rapid equilibration step of H^+ with mobile and fixed buffers. Simulations were carried out in 20-µs time steps with 5-nm shells; similar results were obtained using shorter time steps. Reducing shell thickness and time-step duration had no effect on the levels of pH reached at the core of the cylinder, which is used as a proxy for cylindrical pH equilibration and its level distant from the Hv1 channels. Hydronium diffused at 9.3×10^{-5} cm^2/s (al-Baldawi and Abercrombie, 1992) in the presence of 100 mM MES ($K_D = 7.08\times10^{-7}$ M) and a 85 mM of a fixed buffer, with $K_D = 9.3\times10^{-7}$ M, as in similar mammalian cells (Swietach et al., 2003). Initial pH was buffered to 6.0.

The approximation of an instantaneously equilibrating buffer is justified because the time constant of equilibration of hydrogen buffers (about 0.4 ns, where $1/\tau = k_a([B]+[H]) + k_d$, [B] = 0.1 M, and $k_a = 3x10^{10}$ /M.s from (Nunogaki and Kasai, 1988)) is substantially shorter than the time constant for diffusion (about 20 ns, where $\tau = \delta r^2/4D_{app}$, with δr as the shell thickness and D_{app} is the apparent diffusion constant of hydronium in the presence of fixed and mobile buffers, calculated as $2.8x10^{-6}$ cm^2/s according to (Neher, 1998), with MES diffusing at $8.2x10^{-6}$ cm^2/s according to (Kunkel, 2001). Note that D_{app} is calculated only for this justification and is not used in the actual simulations which account separately for the effects of buffers on diffusion.

For the second *in silico* estimation of the flagellar pH changes under physiological conditions (Fig. S6B) we used the same program and simulation assuming a starting pH of 6.0, and a temperature of 37 °C rather than 25 °C, which should increase hydronium diffusion by 30% (to 1.212×10^{-4} cm^2/s). Assuming that the membrane potential under this condition is around 0 mV, we modified the appropriate outward current of Fig. S1A (right panel) for human sperm using a temperature coefficient Q_{10} of 2.8 for current amplitudes and Q_{10} of 7 for activation time constants (DeCoursey and Cherny, 1998), corresponding to a current rising to 20 pA with a time constant of 59 ms (Lishko et al., 2010). MES was replaced with 30 mM of a native diffusible buffer with $K_D = 2.7\times10^{-8}$ M (Swietach et al., 2003), which would have been replaced in patch clamp experiments with pipette solution.

For the third and final simulation to estimate the steady-state level of pH that might be reached in the neighborhood of a single Hv1 dimer in the presence of buffers (Fig. S6C), we used Excel software to calculate the behavior of the point source solution to the diffusion equation into a semi-infinite space (equation #6 from (De-la-Rosa et al., 2016), as derived by (Nunogaki and Kasai, 1988) and (Decker and Levitt, 1988):

$$c(r) = c_\infty(1 - (a/r)e^{-\lambda(r-a)}), \text{ with } \lambda^2 = k_b[B]/D_H ,$$

where $c(r)$ is the proton concentration in the presence of a rapid buffer, c_∞ is the bulk proton concentration, a is the capture radius of the channel "sink", r is the radial coordinate indicating the vicinity of a proton channel or a distance from the "sink", D_H is the diffusion coefficient of protons in water, [B] is the concentration of buffer, and k_b is the association rate constant. This equation is highly sensitive to a for hydrogen ions (here assumed to be 2 nm, similar to (De-la-Rosa et al., 2016)), and depends on total buffer concentration [B] (185 mM) and on-rate k_b [3×10^{10} /mol·s, from (Nunogaki and Kasai, 1988)] as well as the hydronium diffusion rate D_H (9.3×10^{-5} cm^2/s). Note that $c(r)$ achieves diffusional steady state in a few ns ($\tau = r^2/4D_w$ = 2.7 ns at 10 nm), followed by a smaller and slower phase due to buffer equilibration and diffusion.

The point-source solution involves numerous simplifying assumptions, such as lumping effects of fixed and mobile buffers and the estimate of the Hv1 capture radius. We therefore implemented a diffusion-reaction scheme in spherical coordinates written in BASIC software, similar to the program used in the cylindrical equilibration simulations. This program explicitly included diffusion of both hydronium ions and the native mobile buffer or MES, with a starting pH of 6.0, and instantaneous buffer equilibration was replaced with forward and backward binding reactions for each buffer. The outward current through a single Hv1 cluster was estimated at 39 fA, from the typical whole-sperm proton current divided by the average number of clusters in a sperm tail. Because of the high spatial resolution required, extremely small-time steps were needed to achieve stable and convergent solutions. With 1-nm shells and 0.1-ms time steps, the simulations took 2 full days on a fast computer (3.4 GHz, 8-core Intel i7-6700 processor). The results were similar to those obtained with the point-source equation; for ease of replication and to be consistent with the literature on this subject, we present only the results of the Excel calculations of De-La-Rosa's point source solution (De-la-Rosa et al., 2016).

SI Appendix References:

al-Baldawi, N.F., and Abercrombie, R.F. (1992). Cytoplasmic hydrogen ion diffusion coefficient. Biophys J *61*, 1470-1479.

Chung, J.J., Miki, K., Kim, D., Shim, S.H., Shi, H.F., Hwang, J.Y., Cai, X., Iseri, Y., Zhuang, X., and Clapham, D.E. (2017). CatSperzeζ regulates the structural continuity of sperm Ca^{2+} signaling domains and is required for normal fertility. eLife Feb 23;6. pii: e23082. doi: 10.7554/eLife.23082

Chung, J.J., Shim, S.H., Everley, R.A., Gygi, S.P., Zhuang, X., and Clapham, D.E. (2014). Structurally distinct Ca^{2+} signaling domains of sperm flagella orchestrate tyrosine phosphorylation and motility. Cell *157*, 808-822.

De-la-Rosa, V., Suarez-Delgado, E., Rangel-Yescas, G.E., and Islas, L.D. (2016). Currents through Hv1 channels deplete protons in their vicinity. J of Gen Physiol *147*, 127-136.

Decker, E.R., and Levitt, D.G. (1988). Use of weak acids to determine the bulk diffusion limitation of H+ ion conductance through the gramicidin channel. Biophys J *53*, 25-32.

DeCoursey, T.E., and Cherny, V.V. (1998). Temperature dependence of voltage-gated H+ currents in human neutrophils, rat alveolar epithelial cells, and mammalian phagocytes. J of Gen Physiol *112*, 503-522
.

Huang, B., Wang, W., Bates, M., and Zhuang, X. (2008). Three-dimensional super-resolution imaging by stochastic optical reconstruction microscopy. Science *319*, 810-813.

Kunkel, J.G., Lin, L.Y., Xu, Y., Prado, A.M.M., Feijó, J.A., Hwang, P.P., and Hepler, P.K. (2001). The strategic use of Good buffers to measure proton gradients around growing pollen tubes. In Geitman, A., Cresti, M. and Heath, I.B., Eds. Cell Biology of Plant and Fungal Tip Growth, IOS Press, pps. 81-94.

Lishko, P.V., Botchkina, I.L., Fedorenko, A., and Kirichok, Y. (2010). Acid extrusion from human spermatozoa is mediated by flagellar voltage-gated proton channel. Cell *140*, 327-337.

Lishko, P.V., Botchkina, I.L., and Kirichok, Y. (2011). Progesterone Activates the Principal Ca^{2+} Channel of Human Sperm. Nature *471*, 387-391.

Neher, E. (1998). Usefulness and limitations of linear approximations to the understanding of Ca^{++} signals. Cell Calcium *24*, 345-357.

Nunogaki, K., and Kasai, M. (1988). The H+/OH- flux localizes around the channel mouth in buffered solution. J of Theoret Biol *134*, 403-415.

Pan, L., Yan, R., Li, W., and Xu, K. (2018). Super-Resolution Microscopy Reveals the Native Ultrastructure of the Erythrocyte Cytoskeleton. Cell Rep *22*, 1151-1158.

Rust, M.J., Bates, M., and Zhuang, X. (2006). Sub-diffraction-limit imaging by stochastic optical reconstruction microscopy (STORM). Nat Methods *3*, 793-795.

Smith, J.F., Syritsyna, O., Fellous, M., Serres, C., Mannowetz, N., Kirichok, Y., and Lishko, P.V. (2013). Disruption of the principal, progesterone-activated sperm Ca2+ channel in a CatSper2-deficient infertile patient. Proc Natl Acad Sci USA *110*, 6823-6828.

Swietach, P., Zaniboni, M., Stewart, A.K., Rossini, A., Spitzer, K.W., and Vaughan-Jones, R.D. (2003). Modelling intracellular H(+) ion diffusion. Prog Biophys Mol Biol *83*, 69-100.

Thomas, S.M., and Chan, Y.T. (1989). A simple approach for the estimation of circular arc center and its radius. Computer Vision, Graphics, and Image Processing *45*, 362-370.

Wojcik, M., Hauser, M., Li, W., Moon, S., and Xu, K. (2015). Graphene-enabled electron microscopy and correlated super-resolution microscopy of wet cells. Nat Commun *6*, 7384.

Zhang, M., Kenny, S.J., Ge, L., Xu, K., and Schekman, R. (2015). Translocation of interleukin-1beta into a vesicle intermediate in autophagy-mediated secretion. eLife*;* 5 Nov 2;4. pii: e11205. doi: 10.7554/eLife.11205.